Neutrino energy transport in weak decoupling and big bang nucleosynthesis

E. Grohs,[1,2,*] G. M. Fuller,[1] C. T. Kishimoto,[1,3] M. W. Paris,[4] and A. Vlasenko[1,5]

[1]Department of Physics, University of California, San Diego, La Jolla, California 92093, USA
[2]Department of Physics, University of Michigan, Ann Arbor, Michigan 48109, USA
[3]Department of Physics and Biophysics, University of San Diego, San Diego, California 92110, USA
[4]Theoretical Division, Los Alamos National Laboratory, Los Alamos, New Mexico 87545, USA
[5]Department of Physics, North Carolina State University, Raleigh, North Carolina 27695, USA

(Received 8 December 2015; published 21 April 2016)

We calculate the evolution of the early universe through the epochs of weak decoupling, weak freeze-out and big bang nucleosynthesis (BBN) by simultaneously coupling a full strong, electromagnetic, and weak nuclear reaction network with a multienergy group Boltzmann neutrino energy transport scheme. The modular structure of our code provides the ability to dissect the relative contributions of each process responsible for evolving the dynamics of the early universe in the absence of neutrino flavor oscillations. Such an approach allows a detailed accounting of the evolution of the ν_e, $\bar{\nu}_e$, ν_μ, $\bar{\nu}_\mu$, ν_τ, $\bar{\nu}_\tau$ energy distribution functions alongside and self-consistently with the nuclear reactions and entropy/heat generation and flow between the neutrino and photon/electron/positron/baryon plasma components. This calculation reveals nonlinear feedback in the time evolution of neutrino distribution functions and plasma thermodynamic conditions (e.g., electron-positron pair densities), with implications for the phasing between scale factor and plasma temperature; the neutron-to-proton ratio; light-element abundance histories; and the cosmological parameter $N_{\rm eff}$. We find that our approach of following the time development of neutrino spectral distortions and concomitant entropy production and extraction from the plasma results in changes in the computed value of the BBN deuterium yield. For example, for particular implementations of quantum corrections in plasma thermodynamics, our calculations show a 0.4% increase in deuterium. These changes are potentially significant in the context of anticipated improvements in observational and nuclear physics uncertainties.

DOI: 10.1103/PhysRevD.93.083522

I. INTRODUCTION

In this paper we concurrently solve for the evolution of the neutrino and matter/radiation components in the early universe. A key result of this work is that there is, in fact, nonlinear feedback between these components during the time when the neutrinos go from thermally and chemically coupled with the plasma of photons/electrons/positrons/baryons, to completely decoupled and free streaming. This feedback can be important for high precision calculations of the primordial light element abundances emerging from big bang nucleosynthesis (BBN). The work we describe here builds on the many previous studies of the evolution of the neutrino energy distribution functions in the early universe (see Refs. [1–14] and Appendix A). Higher precision in theoretical calculations of neutrino transport and nucleosynthesis in the early universe is warranted by recent and anticipated improvement in the precision of cosmological observations.

The advent of high precision cosmological observations will demand a deeper understanding and higher precision in modeling the known microphysics of the standard model relevant during the early universe through the neutrino weak decoupling (or simply "weak decoupling") and BBN epochs. For example, future cosmic microwave background (CMB) polarization experiments promise increased sensitivity to issues closely associated with relic neutrino energy distribution functions such as the "sum of the light neutrino masses" and measures of the radiation energy density [15]. Additionally, the advent of extremely large optical telescopes, with adaptive optics, can improve the precision in primordial abundance determinations [16–18].

Leveraging the increased observational precision to achieve better probes of and constraints on beyond standard model (BSM) physics will demand higher precision in simulation of *standard model* physics. Many possible BSM scenarios (e.g. sterile neutrinos, light scalars, out-of-equilibrium particle decay, etc.) could affect weak decoupling and, hence, nucleosynthesis in subtle but potentially measurable ways. Accurate and self-consistent treatments of the standard nuclear and particle physics furthers the objective of a clear interpretation of potential BSM issues (see Refs. [19–21]).

Neutrino kinetics affect the neutrino distributions and primordial nuclide abundances in the early universe in three

*Corresponding author.
egrohs@umich.edu

principal respects. First, the transfer of entropy from the photon/electron/positron plasma to the neutrino seas cools the plasma temperature relative to the case of no transport. The cooler temperature alters the ratio of comoving to plasma energy scales from the canonical value $(4/11)^{1/3} \approx 0.7138$ [22–24].

The second out-of-equilibrium effect is the distortion of the thermal Fermi-Dirac (FD) spectrum of high-energy neutrinos. Upscattering of low-energy neutrinos and the production of neutrino-antineutrino pairs contribute to this distortion through a variety of mechanisms. An important consequence of this mechanism is the effect that the high-energy distortion has on the neutron-to-proton ratio (n/p). A running theme throughout the present study is that such changes induced by the distortion of the neutrino distributions away from equilibrium have effects that must be calculated concurrently with the evolution of the nuclide abundances. In this way, we reveal nonlinearities in feedback mechanisms between the neutrino transport and the thermodynamics of the plasma. These changes to the temperature evolution have an effect on relative changes in the nuclide abundances through the reaction rates and the sensitive dependence of, for example, Coulomb barriers on temperature.

The third out-of-equilibrium effect is entropy production. The Boltzmann H theorem implies that the entropy of a closed system is a nondecreasing function of time. In this paper, we investigate the conventional assumption [22,24] of comoving entropy conservation. We find that there is a small change in the total entropy of the Universe due to the nonequilibrium kinetics of the neutrinos, which generates entropy. In essence, out-of-equilibrium neutrino energy transport and associated entropy flow changes the phasing between scale factor and plasma temperature evolution.

A common feature of past works is that the effect of these transport/entropy issues on the primordial abundances is small, typically on the order of 0.05% for helium-4 and lithium (in particular, see Ref. [7], hereafter DHS). Our work shows that the magnitude of these effects can be significantly larger, depending on assumed microphysics.

The present work employs a nonperturbative method to calculate the evolution of active neutrino occupation probabilities $f_{\nu_i}(p,t)$ for flavor $i = e, \mu, \tau$. Homogeneity and isotropy has been assumed to restrict the dependence of the f_{ν_i} to only the magnitude of the three-momentum p and the comoving time t. The evolution is computed in the presence of two-body to two-body $(2 \to 2)$ collisions, the rates of which are given by the collision integrals $C_{\nu_i}[f_j]$, where f_j refers to the occupation probabilities of neutrinos, antineutrinos, and charged leptons. These are functionals of the set of neutrino and antineutrino occupation probabilities f_{ν_j} and evolve, within the Boltzmann equation approach, as

$$\left[\frac{\partial}{\partial t} - H(a)p\frac{\partial}{\partial p}\right] f_{\nu_i}(p,t) = C_{\nu_i}[f_j], \tag{1}$$

where $H(a)$ is the Hubble expansion rate at scale factor a. We define the independent variable $\epsilon \equiv E_\nu/T_{\rm cm}$ using the neutrino energy E_ν and the comoving temperature parameter $T_{\rm cm}$. The comoving temperature parameter is not a physical temperature. It is simply an energy scale that redshifts like the energy of a massless particle in free fall with the expansion of the Universe and is, in essence, a proxy for inverse scale factor. Therefore, we can write $T_{\rm cm}(a) = T_{\rm in}a_{\rm in}/a(t)$ as a function of scale factor, where $T_{\rm in}$ and $a_{\rm in}$ are the plasma temperature and scale factor at an initial epoch of our choosing. For neutrinos in the range of plasma temperatures 3 MeV $\gtrsim T \gtrsim$ 10 keV, ϵ is equivalent to the commonly used quantity $\tilde{\epsilon} = p/T_{\rm cm}$. Equation (1) can be cast in terms of ϵ as

$$\frac{d}{dt} f_{\nu_i}(\epsilon,t) = C_{\nu_i}[f_j]. \tag{2}$$

The independent variable ϵ is chosen so that energy conservation takes the simple form $\epsilon_1 + \epsilon_2 = \epsilon_3 + \epsilon_4$ for the scattering process $1 + 2 \leftrightarrow 3 + 4$.

The evaluation of the collision integral in Eq. (1) or (2) for the weak-interaction processes of interest is numerically intensive. However, the required integrations (described in detail in Sec. II B 3 and Appendixes B and C) are performed in parallel with the code BURST (BBN/Unitary/Recombination/Self-consistent/Transport) in Fortran 90/95 under OPENMPI. We have developed a routine to evaluate the collision term for the Boltzmann equation in BURST (using methods detailed in the appendixes) which reduce the number of required integrations to two. Numerical integration, effected under a combination of quadrature techniques (detailed in Sec. II), has been tested by ensuring conservation of lepton number; it is satisfied at the level of 10^{-14} (see Sec. II C 2).

The code has been developed to address the problem of weak-decoupling collision terms and for self-consistent coupling to nuclear reactions assuming that a Boltzmann equation treatment is sensible. The "embarrassingly parallel" structure of the problem allows for the simultaneous evaluation of the occupation probabilities f_{ν_i} for each energy, implying a nearly linear scaling of code performance with the number of cores. The present calculational approach is readily generalizable to treat the full neutrino quantum kinetic equations (QKEs) developed in Ref. [25] and therefore neutrino flavor oscillations (see Refs. [26–35] for discussion on the QKEs). As mentioned, the present work neglects neutrino flavor oscillations. A detailed calculation that concurrently solves the neutrino QKE equations, incorporating both effects of flavor oscillations and energy transport, and the primoridal nucleosynthesis is required and currently underway. An example of the need for such a calculation is indicated by the high sensitivity of the n/p ratio at weak freeze-out to the electron neutrino energy distrubtion (see Sec. III). One of the primary effects

of flavor oscillation, whose subsequent effect on primordial nucleosynthesis is difficult to estimate in a self-consistent approach in the dynamic environment of the BBN-epoch of the early universe, is the suppression of the $\nu_e + n \to p + e^-$ rate. This suppression occurs when an electron neutrino oscillates to either a ν_μ or ν_τ state, which do not convert $n \leftrightarrow p$. A detailed, self-consistent calculation will account for the phasings of various such mechanisms, which may be important at the level of precision anticipated for in the next generation of cosmological observations.

We emphasize that we couple neutrino-energy transport self-consistently and concurrently to evaluation of the neutron-to-proton rates and nucleosynthesis reaction network. At each time step in BURST, the weak interaction neutron-proton conversion rates ($n \leftrightarrow p$ rates),

$$\nu_e + n \leftrightarrow p + e^-, \tag{3}$$

$$e^+ + n \leftrightarrow p + \bar{\nu}_e, \tag{4}$$

$$n \leftrightarrow p + e^- + \bar{\nu}_e, \tag{5}$$

are determined using the evolved, nonequilibrium ν_e and $\bar{\nu}_e$ spectra. The thermodynamics of the electromagnetic plasma is coupled to the neutrino seas to account for heat flow between the plasma and the neutrinos. Nonequilibrium effects generate entropy, increasing the total entropy of the plasma and the neutrinos, through a timelike entropy-current flux. Finally, we integrate the neutrino occupation probabilities to determine the energy density for calculating the Hubble expansion rate. In this way, self-consistency within the neutrino sector is maintained over approximately 10^8 Hubble times. The overall architecture employed in BURST differs from the approaches used in previous treatments (see Appendix A).

The nuclear reaction network employed in the current code is based on those of Refs. [36,37] as augmented in Ref. [38]; details are discussed in Ref. [39]. Ongoing work is focused on incorporating into the present approach a nuclear reaction network based on a reaction formalism that respects unitarity.

The outline of this work is as follows. In Sec. II, we present details of the transport code and weak-decoupling calculations. We investigate, in Sec. III, the contributions of the scattering processes to the out-of-equilibrium neutrino spectra. Section IV describes the evolution of the entropy during the weak-decoupling process. Section V discusses primordial nucleosynthesis resulting from the self-consistent coupling to the transport code. We conclude in Sec. VI. Appendix A contains a summary of the calculations of different groups. Appendixes B and C describe the analytical derivations of the collision terms. We should emphasize that the current manuscript represents a preliminary step toward the objective of coupling neutrino kinetics to the nucleosynthesis reaction network. The proper treatment of neutrino flavor oscillations and possible coherent effects requires a quantum kinetic approach [25]. Flavor oscillations have been estimated [12] to change the production of ^{4}He at the 20% level. The self-consistent approach that we consider here might be expected to enhance this change; a detailed calculation is required to estimate the actual effect. We detail further ongoing efforts in this work in the conclusion, Sec. VI. Throughout this paper we use natural units where $\hbar = c = k_B = 1$.

In this manuscript we have provided a pedagogical presentation of some familiar topics. This is done in the interest of giving a clear presentation of our work and in the hopes of making our analytical and numerical computations reproducible.

II. NEUTRINO WEAK DECOUPLING CALCULATIONS

Neutrinos decouple from the plasma, roughly speaking, when typical rates of the weak processes, Γ_w given in Table I, fall below the Hubble rate:

$$\frac{\Gamma_w}{H} \lesssim \frac{G_F^2 T^5}{T^2/m_{\rm Pl}} \simeq \left(\frac{T}{0.7\ {\rm MeV}}\right)^3, \tag{6}$$

where $G_F = 1.166 \times 10^{-11}\ {\rm MeV}^{-2}$ is the Fermi constant and $m_{\rm Pl} = 1.221 \times 10^{22}$ MeV. By numerically evolving the neutrino distributions for ν_e, $\bar{\nu}_e$, ν_μ, $\bar{\nu}_\mu$, ν_τ, and $\bar{\nu}_\tau$ we find, however, that the neutrinos exchange entropy with the plasma until a temperature of nearly 100 keV—many Hubble times beyond the estimate in Eq. (6) (see Fig. 9). This is in part explained by the fact that given the large entropy of the early universe, which is carried by both photons/electrons/positrons and neutrinos, a significant fraction of the neutrinos have energies larger than the temperature. This effect is enhanced by plasma particles scattering from the neutrinos, which preferentially upscatter the neutrinos and distort the high-momentum tails of the neutrino distributions. In this section, we present the details of the numerical evaluation of the collision integrals, the solution of the Boltzmann equation, and performance statistics of the code, followed by details of the weak decoupling calculations.

A. Weak interaction processes

We discuss the weak interactions relevant for neutrino weak decoupling here and their implementation in the collision integral C in the Boltzmann equation, Eq. (1).

Expressions for the neutral and charged current weak interaction processes involving neutrinos, antineutrinos and the charged leptons of the plasma are given in Table I. The table gives the squared amplitudes $\langle|\mathcal{M}_r|^2\rangle$, where r labels two-body processes that are important during neutrino weak decoupling [40,41], averaged over initial spin states and summed over final spins. The initial state particle four-momenta in Table I are given particle numbers 1 and 2; final states are 3 and 4. That is

TABLE I. Weak interaction processes relevant for neutrino weak decoupling. The left column labels the scattering, production, and annihilation processes in the middle column by an index r. The right column gives the spin-averaged and summed square of the matrix element $\mathcal{M}_r$ for process r with the Fermi constant and symmetry factor S_r divided out. Indices i and j in the middle column for processes $r = 1, \ldots, 5$, which describe neutrino and antineutrino scattering, are distinct. Processes with an antineutrino scattering on a charged lepton, correspond to the parity-conjugate reactions of $r = 6, \ldots, 9$. Since they have identical matrix elements to these they are not shown in the table, although their effect is explicitly accounted for in antineutrino energy transport. S_r is unity for all processes except $r = 1$, where $S_1 = 1/2$.

r	Process	$G_F^{-2} S_r \langle \lvert\mathcal{M}_r\rvert^2 \rangle$
1	$\nu_i + \nu_i \leftrightarrow \nu_i + \nu_i$	$2^6 (P_1 \cdot P_2)(P_3 \cdot P_4)$
2	$\nu_i + \nu_j \leftrightarrow \nu_i + \nu_j$	$2^5 (P_1 \cdot P_2)(P_3 \cdot P_4)$
3	$\nu_i + \bar{\nu}_i \leftrightarrow \nu_i + \bar{\nu}_i$	$2^7 (P_1 \cdot P_4)(P_2 \cdot P_3)$
4	$\nu_i + \bar{\nu}_j \leftrightarrow \nu_i + \bar{\nu}_j$	$2^5 (P_1 \cdot P_4)(P_2 \cdot P_3)$
5	$\nu_i + \bar{\nu}_i \leftrightarrow \nu_j + \bar{\nu}_j$	$2^5 (P_1 \cdot P_4)(P_2 \cdot P_3)$
6	$\nu_e + e^- \leftrightarrow e^- + \nu_e$	$2^5[(2\sin^2\theta_W + 1)^2 (P_1 \cdot Q_2)(Q_3 \cdot P_4) + 4\sin^4\theta_W (P_1 \cdot Q_3)(Q_2 \cdot P_4) - 2\sin^2\theta_W (2\sin^2\theta_W + 1) m_e^2 (P_1 \cdot P_4)]$
7	$\nu_{\mu(\tau)} + e^- \leftrightarrow e^- + \nu_{\mu(\tau)}$	$2^5[(2\sin^2\theta_W - 1)^2 (P_1 \cdot Q_2)(Q_3 \cdot P_4) + 4\sin^4\theta_W (P_1 \cdot Q_3)(Q_2 \cdot P_4) - 2\sin^2\theta_W (2\sin^2\theta_W - 1) m_e^2 (P_1 \cdot P_4)]$
8	$\nu_e + e^+ \leftrightarrow e^+ + \nu_e$	$2^5[(2\sin^2\theta_W + 1)^2 (P_1 \cdot Q_3)(Q_2 \cdot P_4) + 4\sin^4\theta_W (P_1 \cdot Q_2)(Q_3 \cdot P_4) - 2\sin^2\theta_W (2\sin^2\theta_W + 1) m_e^2 (P_1 \cdot P_4)]$
9	$\nu_{\mu(\tau)} + e^+ \leftrightarrow e^+ + \nu_{\mu(\tau)}$	$2^5[(2\sin^2\theta_W - 1)^2 (P_1 \cdot Q_3)(Q_2 \cdot P_4) + 4\sin^4\theta_W (P_1 \cdot Q_2)(Q_3 \cdot P_4) - 2\sin^2\theta_W (2\sin^2\theta_W - 1) m_e^2 (P_1 \cdot P_4)]$
10	$\nu_e + \bar{\nu}_e \leftrightarrow e^- + e^+$	$2^5[(2\sin^2\theta_W + 1)^2 (P_1 \cdot Q_4)(P_2 \cdot Q_3) + 4\sin^4\theta_W (P_1 \cdot Q_3)(P_2 \cdot Q_4) + 2\sin^2\theta_W (2\sin^2\theta_W + 1) m_e^2 (P_1 \cdot P_2)]$
11	$\nu_{\mu(\tau)} + \bar{\nu}_{\mu(\tau)} \leftrightarrow e^- + e^+$	$2^5[(2\sin^2\theta_W - 1)^2 (P_1 \cdot Q_4)(P_2 \cdot Q_3) + 4\sin^4\theta_W (P_1 \cdot Q_3)(P_2 \cdot Q_4) + 2\sin^2\theta_W (2\sin^2\theta_W - 1) m_e^2 (P_1 \cdot P_2)]$

$$1 + 2 \leftrightarrow 3 + 4, \tag{7}$$

where particle 1 is always a neutrino (or antineutrino). We label neutrino four-momenta as P_i and charged lepton four-momenta as Q_i.

The $\langle \lvert\mathcal{M}_r\rvert^2 \rangle$ are different for electron-flavor neutrinos compared to μ or τ-flavor neutrinos due to the charged-current interaction, which alters the factor $2\sin^2\theta_W - 1$ to $2\sin^2\theta_W + 1$.[1] The Weinberg angle θ_W is taken as $\sin^2\theta_W \approx 0.23$. At the energy scales of interest here the μ and τ neutrino species have the same interactions.

1. Collision integrals

Given the amplitudes $\mathcal{M}_r$ of Table I, we may calculate the collision integral of Eq. (1):

$$C_{\nu_1}^{(r)}[f_j] = \frac{1}{2E_1} \int \frac{d^3p_2}{(2\pi)^3 2E_2} \frac{d^3p_3}{(2\pi)^3 2E_3} \frac{d^3p_4}{(2\pi)^3 2E_4} \times (2\pi)^4 \delta^{(4)}(P_1 + P_2 - P_3 - P_4) S_r \langle \lvert\mathcal{M}_r\rvert^2 \rangle \times F_r(p_1, p_2, p_3, p_4), \tag{8}$$

where S_r is the symmetrization factor for identical particles, and

$$F_r(p_1, p_2, p_3, p_4) = [1 - f_1][1 - f_2] f_3 f_4 - f_1 f_2 [1 - f_3][1 - f_4], \tag{9}$$

$$= F_r^{(+)} - F_r^{(-)}. \tag{10}$$

Here we have suppressed time dependence and written the occupation probability functions in abbreviated form. For example, f_1 for $r = 1$ would read $f_{\nu_1}(p_1, t)$. The quantities $F_r^{(\pm)}$, corresponding to the first and second lines of Eq. (9), give the probability for scattering into $(+)$ or out of $(-)$ the phase space volume for particle "1"; they include Pauli blocking factors $\sim(1 - f_i)$. The phase space measure for particles 2, 3, and 4, and the arguments of the four-momentum conserving delta function $\delta^{(4)}(P_1 + P_2 - P_3 - P_4)$ and of F_r are written schematically with the dependence of p_i on r, which can either be four-momentum P_i or Q_i, suppressed. The factor $(2E_1)^{-1}$ ensures that an integral over $d^3p_1/(2\pi)^3$ of the collision integral for f_1 vanishes in number-conserving processes; this is discussed in more detail in Sec. II C. All amplitudes in Table I are proportional to G_F, the Fermi coupling constant. The square of the Fermi coupling and a factor of $T_{\rm cm}^5$ may be taken outside of the collision integral [Eq. (8)] to give a dimensionless expression with integration variable ϵ, the binning parameter for the occupation probabilities. The product $G_F^2 T_{\rm cm}^5$ has dimensions of energy or inverse time, appropriate to that for a rate. The expression for the collision integral appearing in Eq. (1) is

$$C_{\nu_i}[f_j] = \sum_r C_{\nu_i}^{(r)}[f_j] \tag{11}$$

for processes r that include ν_i.

[1] We note some typographical differences between Table I and Tables I and II in DHS. Row 10 here corresponds to Row 6 of Table I in DHS. While the expression $G_F^{-2} S_6 \langle \lvert\mathcal{M}_6\rvert^2 \rangle$ is the same as that of DHS, the third particle [see Eq. (7)] in our row 10 is an electron, and the third particle of row 6 in Table I of DHS is a positron, which should result in a different expression. This discrepancy also occurs between our row 11 and row 6 of Table II in DHS. Our expression for $r = 10$, however, agrees with that of row 7 of Table I in Ref. [6].

In general, for $2 \to 2$ processes, Eq. (8) is a nine-dimensional integral over the phase space of particles 2, 3, and 4. The four-momentum conserving δ function reduces the collision integral to five dimensions. Homogeneity and isotropy further reduce Eq. (8) to a two-dimensional expression in terms of single-particle energies of either species 2 and 3, or 2 and 4, or 3 and 4. The method of the reduction to two dimensions is distinct from and independent of that of DHS. The reduction is tuned for the specific process in Table I to ensure speed and accuracy in a parallel computation. Appendix B details our straightforward but lengthy method to obtain the two-dimensional expression for the process in the first row of Table I. Appendix C gives the reduction algorithm for collision integrals for the remaining processes of Table I. In both appendixes, we relabel the indices of the active particle species in Table I to simplify the presentation.

B. Numerical evaluation

In the interest of providing a complete description of the numerical evaluation of the collision integrals of Eq. (8) we describe here our choices for the energy (ϵ) binning, numerical quadrature, interpolation and extrapolation, and convergence criteria.

1. Binning

We employ a linear binning scheme for the occupation probabilities in terms of the comoving invariant quantity $\epsilon = E_\nu/T_{\rm cm}$. The interval from $\epsilon = 0$ to $\epsilon = \epsilon_{\rm max}$ is partitioned into $N_{\rm bins}$ equal-width bins. For a linear binning scheme, we use $N_{\rm bins} + 1$ abscissas with the lowest abscissa at $\epsilon = 0$. The $\epsilon_{\rm max}$ must be chosen large enough to support the f_{ν_i} and $f_{\bar{\nu}_i}$. We compare the numerically integrated equilibrium energy spectrum to the analytical FD calculation at high temperature and find agreement to a few parts in 10^6.

We have performed test calculations with values of $N_{\rm bins}$ from 100 to 1000. The computing time has been verified empirically to scale as $N_{\rm bins}^3$. Computation of the nuclear reaction network and thermodynamic quantities associated with charged leptons and photons incurs minimal computational overhead. Parallel code implementation of the calculations results in reasonable wall-clock times $\sim$ days on $\mathcal{O}(100)$ processors even with fine ϵ binning. Typically, we find convergence for $N_{\rm bins} = 100$, as discussed later in this section.

2. Charged lepton quantities

For the processes relevant to weak decoupling, the occupation probabilities for the charged leptons are required. We assume these are given by the FD equilibrium spectra with chemical potential μ and temperature T:

$$f_{e^\pm}(E, T, \mp\mu) = \frac{1}{\exp\left(E/T \pm \phi_e\right) + 1}, \tag{12}$$

where $\phi_e = \mu/T$ is the electron degeneracy parameter. Here ϕ_e is determined by the requirement of charge neutrality in the electron/positron/baryon plasma. We assume zero lepton number residing in the neutrino seas[2] and neglect neutrino-nucleon charged-current transfer of electron lepton number between the electrons/positrons and electron neutrino/antineutrinos. This is plausible since the baryon-to-photon ratio is small. Finite electron mass is taken into account in Eq. (12) where $E = \sqrt{p^2 + m_e^2}$. We define, for future use, the scaled mass m_ϵ as

$$m_\epsilon \equiv \frac{m_e}{T_{\rm cm}}. \tag{13}$$

We employ the comoving temperature, as its evolution is simple.

3. Numerical quadrature

Upon reduction of the three-body, nine-dimensional momentum integrals as detailed in Appendix B, we may effect the remaining momentum integrations, which are transformed to integrals over ϵ, via numerical quadrature. We refer to the integration performed first (second) as "inner" ("outer"). We neglect the neutrino rest mass and divide the energy (or, equivalently, momentum) variable by $T_{\rm cm}$ to obtain the variables ϵ_i, where i refers to either inner or outer integrations. If the integral is over a charged-lepton kinematic variable, we use its energy. The squared-amplitude expressions require both energies and three-momenta. We determine dimensionless momenta as $p/T_{\rm cm} = \sqrt{\epsilon^2 - m_\epsilon^2}$, where m_ϵ is given in Eq. (13).

Depending on the specific process in Table I, the ϵ integral may be over a neutrino or a charged lepton. For the inner integral, irrespective of the species, the integration method is a Gaussian quadrature method [42]. When the limits of the inner integral are finite, we use Gauss-Legendre. For finite intervals over a range of ϵ larger than 200 and semi-infinite intervals, we use Gauss-Laguerre.

When the outer integral is over an ϵ-value of a charged lepton, we use either a Gauss-Legendre or Gauss-Laguerre method, depending on the integration limits. In the case that the outer integral is over a neutrino energy, we use a five-point (Boole's) rule [43] with abscissas aligned with the bin points. This affords a slight improvement in performance by avoiding interpolation for this integration of the occupation probabilities for the neutrino energy of the outer integral.

[2]Our approach allows nonzero lepton asymmetry. The assumption of zero neutrino lepton number is stipulated for the present work and is in accord with the standard model.

4. Interpolation and extrapolation

As detailed in Appendix C, we have the freedom to choose which single-particle ϵ-values to use in calculating the collision integral. The $2 \to 2$ processes in Table I have at least two neutrinos in the combined initial and final states. We use three of the four energy- or momentum-conserving δ functions to eliminate an integral over the phase space of one of the neutrino species. This procedure requires an interpolation over the ϵ-value of that species to determine the occupation probability. Processes that involve four neutrinos or antineutrinos require an additional interpolation over ϵ for the occupation probability of the inner integration variable species. The outer integration is either a Gaussian quadrature method over a charged lepton, or a Boole's rule method over the bin points. In either case, no interpolation is required. There is no situation in which we need to interpolate the occupation probabilities for the charged leptons since they are given by the equilibrium FD expressions for electrons and positrons.

We use a fifth-order polynomial interpolator [43] for the neutrino occupation probabilities if the energy of the third or fourth neutrino does not fall on an abscissa. The accuracy of this interpolation is better if we interpolate on the logarithms of the occupation probabilities, as opposed to the occupation probabilities themselves. The domain of integration is extended beyond $\epsilon_{\rm max}$, to $\epsilon = 300$, by extrapolation. Beyond this point the occupation probability is taken to be zero. None of our results are sensitive to these extrapolations.

5. Acceptance tolerance for rates

When the occupation probabilities f_i in Eq. (9) are all equilibrium-distribution values, the collision integral is zero, independent of the value of the squared matrix elements. Numerical quadrature and interpolation, however, incur errors at the precision limitations of these methods and the collision integrals attain small values when calculated under equilibrium conditions. During the computation the need arises to set the tolerance to accept a collision integral value as nonzero or, conversely, to reject a value as the result of imprecision. To accomplish this task, we use the net rate and forward-reverse-summed (FRS) rate. The net rate is the value given by the collision integral in Eq. (8). The FRS rate corresponds to the sum of contributions to the collision integral by substituting $F_r^{(+)} + F_r^{(-)}$ for F_r [Eq. (9)] into Eq. (8).

We calculate the net and FRS rates for each neutrino and antineutrino species in each bin for all processes $r = 1, \ldots, 11$ (and the antineutrino versions of interactions $r = 6, \ldots, 9$) in Table I assuming thermal and chemical equilibrium between the three flavors of neutrinos, antineutrinos, positrons and electrons. We sum over all of the processes to obtain the collision integral for the net rate, and a modified collision integral for the FRS rate. For each neutrino species and each bin, we calculate the precision ratio, defined as

$$\mathcal{R}_{\nu_i}(\epsilon) \equiv \frac{|C_{\nu_i}[f_j^{(\rm eq)}(\epsilon)]|}{C_{\nu_i}[f_j^{(\rm eq)}(\epsilon)]_{\rm FRS}}, \tag{14}$$

where $f_j^{(\rm eq)}(\epsilon)$ is the equilibrium FD occupation probability for species j at a given ϵ bin. The FRS rate is numerically strictly positive. The absolute value of the net rate is required to obtain a strictly positive precision ratio since negative values can arise in and near equilibrium due to finite numerical precision. For diagnostic purposes only (i.e., not in our transport calculations) we take $m_e = 0$, meaning no temperature dependence in Eq. (14).

In production runs of BURST, during weak decoupling, we calculate the collision integrals for both the net and FRS rates at each time step. We compare the ratio of values of the net and FRS rates for the evolved, in general non-equilibrium distributions f_i, to those of the equilibrium distributions [Eq. (14)]. If the ratio in (14) is larger than the tolerance threshold

$$\left\{\frac{|C_{\nu_i}[f_j(\epsilon)]|}{C_{\nu_i}[f_j(\epsilon)]_{\rm FRS}}\right\} \Big/ \mathcal{R}_{\nu_i}(\epsilon) > \varepsilon(\text{net/FRS}), \tag{15}$$

the collision integral is accepted as nonzero and used in the evaluation of the time derivative of the occupation probability $f_i(\epsilon)$. If the left-hand side of Eq. (15) is smaller than the threshold, we set the collision integral to zero. The precision ratio $\mathcal{R}_{\nu_i}(\epsilon)$ never gets larger than a few parts in 10^{12}.

C. Conservation sum rules

We have tested the convergence of the numerical quadrature of the collision integrals by studying number and energy sum rules. Accurate evaluation of the collision integral is necessary to maintain the conservation of energy-momentum, particle number (for species with conserved charges), and neutrino lepton number. These are discussed in the following two sections.

1. Number and energy sum rules

We define the total scaled errors in the number and energy densities as

$$\delta\left(\frac{dn}{dt}\right) = \frac{\sum_\nu \int d\epsilon \epsilon^2 \left.\frac{df_\nu}{dt}\right|_{\rm net}}{\sum_\nu \int d\epsilon \epsilon^2 \left.\frac{df_\nu}{dt}\right|_{\rm FRS}}, \tag{16}$$

$$\delta\left(\frac{d\rho}{dt}\right) = \frac{\sum_\nu \int d\epsilon \epsilon^3 \left.\frac{df_\nu}{dt}\right|_{\rm net}}{\sum_\nu \int d\epsilon \epsilon^3 \left.\frac{df_\nu}{dt}\right|_{\rm FRS}}, \tag{17}$$

respectively. The summation over ν is for the three flavors of neutrinos and antineutrinos and the denominators in these expressions are strictly positive. We evaluate the sum rules including contributions only from processes isolated within the neutrino seas, i.e., $r = 1, 2, \ldots, 5$ in Table I to gauge the effectiveness of the numerical evaluation in respecting number and energy conservation. The spectra of the charged leptons are assumed to be described by equilibrium distributions so scattering processes involving electrons and positrons will not preserve the sum rules as written in Eqs. (16) and (17).

The neutrinos are assumed, in our computational approach, to be in thermal equilibrium with the electrons and positrons until a temperature $T_{\rm in} \gg 1$ MeV. The comoving temperature and plasma temperature are equal for all temperatures greater than the input temperature: $T = T_{\rm cm} \geq T_{\rm in}$. At $T_{\rm in}$, we commence evaluation of the collision integrals and evolve the neutrino occupation probabilities until a comoving temperature $T_{\rm stop}$. The computation approach adopted in BURST utilizes an adaptive Cash-Karp [43] time step. It evolves observables at $\sim 3 \times 10^4$ steps on the interval defined by $T_{\rm in}$ and $T_{\rm stop}$ with a fifth-order Runge-Kutta (RK5) algorithm. All simulations in this paper have $\epsilon_{\rm max} = 20.0$, $N_{\rm bins} = 100$, $T_{\rm in} = 8$ MeV, and $\varepsilon({\rm net/FRS}) = 30.0$. The terminal temperature is $T_{\rm stop} = 15$ keV, corresponding to a plasma temperature of $T \sim 20$ keV. In thermal equilibrium, the total scaled errors are small but nonzero and evaluate to $\sim 10^{-12}$ for both the number and energy sum rules for 100 bins.

We monitor the total scaled errors of Eqs. (16) and (17) at each time step during our weak decoupling calculations. On average, we maintain accuracy to better than one part in 10^6 over the entire run.

2. Neutrino lepton number conservation

Elastic processes satisfy

$$\int d^3 p C^{(r)}_{\nu_i}(p) = 0, \tag{18}$$

since the processes $r = 1, \ldots, 4$ and $r = 6, \ldots, 9$ (and their antineutrino counterparts) conserve neutrino (antineutrino) number. The annihilation processes, $r = 5$, 10 and 11 satisfy, for example

$$\int d^3 p [C^{(\nu_e\bar{\nu}_e,\nu_\mu\bar{\nu}_\mu)}_{\nu_e}(p) - C^{(\nu_e\bar{\nu}_e,\nu_\mu\bar{\nu}_\mu)}_{\bar{\nu}_e}(p)] = 0, \tag{19}$$

$$\int d^3 p [C^{(\nu_e\bar{\nu}_e,\nu_\mu\bar{\nu}_\mu)}_{\nu_\mu}(p) - C^{(\nu_e\bar{\nu}_e,\nu_\mu\bar{\nu}_\mu)}_{\bar{\nu}_\mu}(p)] = 0. \tag{20}$$

Analogous relations hold for other annihilation processes that fall under the reaction classes $r = 5$, 10 and 11.

We have confirmed that the neutrino lepton numbers are conserved at the level of $\lesssim 10^{-14}$ for all values of the scale factor $a(t)$.

III. RESULTS IN THE NEUTRINO SECTOR

Our treatment of the Boltzmann-equation evolution of the neutrino energy transport reveals novel features of the transport characteristics of the active neutrino sector. We focus first on these results, which are largely independent of the coupling to BBN through the nuclear reaction network. The present calculations reveal, in particular, that the history of $e^\pm$ annihilation to photons displays a rich set of behaviors that has not been discussed before. We also look into the role of QED radiative corrections. These results are in line with previous work but they indicate that a more comprehensive treatment of the plasma physics during the epochs we consider is warranted.

A. Neutrino interactions and energy transport

Table II summarizes the neutrino energy transport properties in the present calculations, which as mentioned are carried out for computational parameters $\epsilon_{\rm max} = 20.0$, $N_{\rm bins} = 100$, $T_{\rm in} = 8$ MeV, $T_{\rm stop} = 15$ keV, and $\varepsilon({\rm net/FRS}) = 30.0$. In this section, we focus on the first row of the table, when all of the weak interactions of neutrinos (and the antineutrino reactions corresponding to the parity conjugates of the reactions $r = 6, \ldots, 9$) are computed. We discuss the results for selective process evaluations corresponding to the remaining rows of this table in the next section, Sec. III B. We briefly describe this table to orient the subsequent discussion.

The first column of Table II lists the processes r from Table I used for a given run. The second column gives the

TABLE II. Process-dependent changes in neutrino energy density properties. For all runs $\epsilon_{\rm max} = 20.0$, $N_{\rm bins} = 100$, $T_{\rm in} = 8$ MeV, $T_{\rm stop} = 15$ keV, $\varepsilon({\rm net/FRS}) = 30.0$. The first column gives the processes used for a given run. The second column is the ratio of comoving to plasma temperature. For column two reference, $(4/11)^{1/3} = 0.7138$. Columns three and four are the relative changes of the ν_e and ν_μ energy densities. The quantity $\Delta N_{\rm eff}$ is given by Eq. (24). Round-off error of the neglected fifth significant digit in columns 2, 3, and 4 accounts for the one part in 10^4 discrepancy with column 5.

Processes	$T_{\rm cm}/T$	$100 \times \delta\rho_{\nu_e}$	$100 \times \delta\rho_{\nu_\mu}$	$\Delta N_{\rm eff}$
All	0.7148	0.9282	0.3771	0.03397
10, 11	0.7147	0.9383	0.2867	0.03063
1, 2, 10, 11	0.7147	0.9268	0.2963	0.03078
1, 2, 3, 4, 5, 10, 11	0.7147	0.8557	0.3465	0.03136
6, 7, 8, 9	0.7140	0.1853	0.0639	0.00723
1, 2, 6, 7, 8, 9	0.7140	0.1724	0.0778	0.00753
1, 2, 3, 4, 5, 6, 7, 8, 9	0.7140	0.1559	0.0886	0.00763

ratio of the comoving to plasma temperatures. Columns three and four give the relative changes of the ν_e and ν_μ energy densities, respectively, with respect to the equilibrium energy density:

$$\delta\rho_{\nu_i} \equiv \frac{\rho_{\nu_i} - \rho_\nu^{(\mathrm{eq})}}{\rho_\nu^{(\mathrm{eq})}}, \qquad \rho_\nu^{(\mathrm{eq})} = \frac{7}{8}\frac{\pi^2}{30} T_{\mathrm{cm}}^4. \tag{21}$$

The last column is the change in N_{eff}. N_{eff} is defined through the energy density in ultrarelativistic particles—the radiation energy density $\rho_{\mathrm{rad}}(a)$—after the epoch of photon decoupling as

$$\rho_{\mathrm{rad}}(a_{\gamma d}) = \left[2 + \frac{7}{4}\left(\frac{4}{11}\right)^{4/3} N_{\mathrm{eff}}\right]\frac{\pi^2}{30} T_{\gamma d}^4, \tag{22}$$

where $a(t)$ is the scale factor at universal comoving time t, $T(a)$ is the plasma or photon temperature and $T_{\gamma d} = T(a_{\gamma d})$ is the photon temperature at the conclusion of the epoch of photon decoupling. We make the assumption that T_{cm}/T and $\delta\rho_{\nu_i}$ do not change significantly for 10 keV $\gtrsim T \gtrsim$ 0.2 eV. Therefore, if we set the radiation energy density equal to the sum of the photon and neutrino densities in Eq. (22), we can determine N_{eff} from T_{cm}/T and $\delta\rho_{\nu_i}$:

$$N_{\mathrm{eff}} = \left[\frac{(T_{\mathrm{cm}}/T_{\gamma d})}{(4/11)^{1/3}}\right]^4 \times [(1+\delta\rho_{\nu_e}(a_{\gamma d})) + 2(1+\delta\rho_{\nu_\mu}(a_{\gamma d}))]. \tag{23}$$

In writing Eq. (23), we have assumed that antineutrinos have the same relative change in energy density as neutrinos. The change in N_{eff} is given as

$$\Delta N_{\mathrm{eff}} = N_{\mathrm{eff}} - 3, \tag{24}$$

where N_{eff} is given by Eq. (23). It is clear from this table that the dominant contribution to the parameter ΔN_{eff} is due to annihilation processes $r = 10$ and 11. Additionally, for $\Delta N_{\mathrm{eff}} \sim 0.05$, the value typically quoted in the literature [13], the effect of charged lepton scattering is small but not negligible.

Another feature apparent in Table II is nonlinearity in the combination of processes. Adding, for example, the values of ΔN_{eff} for Table II rows 4 and 5, which sums all of the processes $r = 1, \ldots, 11$ (and the implied charged-lepton antineutrino scattering processes) with $\Delta N_{\mathrm{eff}} = 0.039$ is not equivalent to the Table II first row with $\Delta N_{\mathrm{eff}} = 0.034$. Finally, the ratio of the comoving temperature to the plasma temperature T_{cm}/T is largely set by the annihilation processes. We note, however, that this does not uniquely determine ΔN_{eff} as Eq. (22) implies.

Figures 1 to 4 show relative changes in the neutrino spectra for a calculation with transport versus a no-transport calculation. All processes are active in the transport calculation, i.e. row 1 of Table II. The no transport calculation maintains FD-like distributions at temperature parameter T_{cm}. We compare our present results, in detail, to DHS and Ref. [11]. To this end, we first define several quantities to facilitate this comparison and then turn to a detailed discussion of each of these figures.

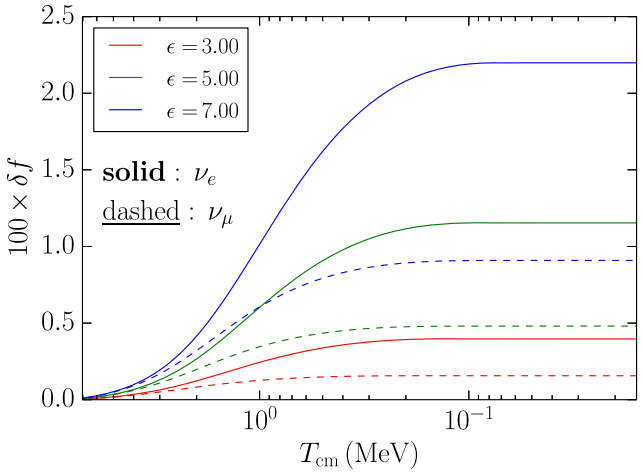

FIG. 1. The relative change, as in Eq. (25), in the occupation probability as a function of the comoving temperature T_{cm}. Three values of ϵ are evaluated at $\epsilon = 3$, 5 and 7. The solid lines are for electron-flavor neutrinos, and the dashed lines are for muon-flavor neutrinos. The larger δf correspond to larger ϵ values.

We define δf at a given time t and ϵ to be the relative change in the occupation probabilities with respect to the FD occupation probability:

$$\delta f \equiv \frac{f(\epsilon, t) - f^{(\mathrm{eq})}(\epsilon)}{f^{(\mathrm{eq})}(\epsilon)} \tag{25}$$

where

$$f^{(\mathrm{eq})}(\epsilon) = \frac{1}{e^\epsilon + 1}. \tag{26}$$

We note that $f^{(\mathrm{eq})}$ does not depend explicitly on time or temperature. Figures 1 and 2 show δf as a function, respectively, of T_{cm} for $\epsilon = 3$, 5 and 7 and as a function of ϵ at a comoving temperature $T_{\mathrm{cm}} = 1$ keV. Figure 3 displays the difference in the relative change for neutrinos and antineutrinos:

$$\delta\bar{f} \equiv \delta f_\nu - \delta f_{\bar{\nu}} = \frac{f_\nu - f_{\bar{\nu}}}{f^{(\mathrm{eq})}}. \tag{27}$$

Figure 4 shows the normalized change in the differential energy density:

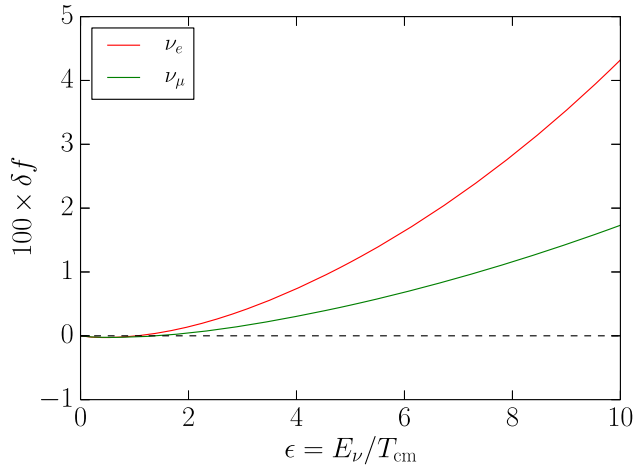

FIG. 2. The relative change, as in Eq. (25), in the occupation probability as a function of ϵ for $T_{\rm cm} = 1$ keV. The larger change is the electron-flavor neutrinos, over the muon-flavor neutrinos. The antineutrino evolution is nearly identical to the neutrino evolution for all flavors.

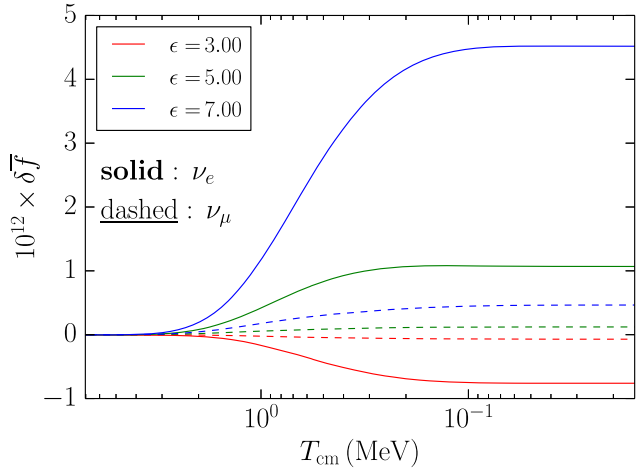

FIG. 3. The difference in relative changes in the occupation probabilities of ν and $\bar{\nu}$ [Eq. (27)] as a function of comoving temperature $T_{\rm cm}$. Three values of ϵ are plotted at $\epsilon = 3$, 5 and 7. The solid lines are for electron-flavor neutrinos, and the dashed lines are for muon-flavor neutrinos. The ν_e experience a larger change than the ν_μ.

$$\frac{\Delta(\frac{d\rho}{d\epsilon})}{\rho} = \frac{[\frac{\epsilon^3}{2\pi^2} f(\epsilon) - \frac{\epsilon^3}{2\pi^2} f^{(\rm eq)}(\epsilon)]}{\frac{1}{2\pi^2}\int dx x^3 f^{(\rm eq)}(x)} \tag{28}$$

$$= \frac{120}{7\pi^4}\epsilon^3 [f(\epsilon) - f^{(\rm eq)}(\epsilon)]. \tag{29}$$

The antineutrino behavior is nearly identical to the neutrino behavior for all flavors.

For each ϵ-value in Fig. 1 the relative change in the electron-flavor (ν_e) is larger than the relative change in the muon-flavor (ν_μ) neutrino sea. The annihilation and scattering rates with electrons and positrons are faster due to the contribution of the charged-current diagrams for ν_e, which are absent for ν_μ, as noted in Ref. [11]. In addition to the larger affect on the ν_e spectra, the charged-current processes keep the ν_e in thermal contact with the charged leptons longer than ν_μ. This is apparent from Fig. 1 where freeze-out corresponds to the point where the derivative of the curves goes to zero. The ν_μ freeze-out occurs at an earlier epoch than the ν_e freeze-out. Additionally, freeze-out occurs later for larger ϵ values, as noted in DHS. These results are generally consistent with DHS and Ref. [11]. For example, the $\epsilon = 5$, ν_e curve rises at a more rapid rate than, and crosses, the $\epsilon = 7$, ν_μ curve. Figure 4 of Ref. [11] also exhibits this crossing between the $\epsilon = 5$, ν_e curve and the $\epsilon = 7$, ν_μ curve. Comparing Fig. 1 with Figs. 3(a) and 3(b) of DHS confirms the similar behavior of BURST and DHS.

Figure 2, plotted at a temperature of $T_{\rm cm} = 1$ keV well after weak decoupling, shows that the ν_e have a larger distortion than the ν_μ and that this effect is enhanced at large ϵ. An interesting feature of Fig. 2 is the negative relative change for $\epsilon \lesssim 1$. It appears to occur in Fig. (5) of both DHS and Ref. [11] but is not explicitly mentioned in either reference. We investigate this phenomenon in more detail in the subsections below. In addition, our relative changes are in good agreement with those of DHS for both ν_e and ν_μ.

In Fig. 3, we exhibit the difference in the relative change of ν_e and $\bar{\nu}_e$, and also ν_μ and $\bar{\nu}_\mu$. The electron-flavor shows an enhanced effect over the muon-flavor for all ϵ-values. For both flavors, at ϵ-values $= 5$ and 7 in Fig. 3, the relative changes are positive. The negative differences for $\epsilon = 3$ indicate there is an abundance of antineutrinos over neutrinos, independent of flavor. The differences between neutrino and antineutrino distributions for both e and μ are small for all epsilon values considered here. This raises, however, the important issue of how neutrino flavor evolves under the full quantum kinetic evolution [25].

Figure 4 shows where the largest change in the energy-density spectrum occurs. Figure 4 is approximately equivalent to Fig. 2 multiplied by $\epsilon^3 f^{(\rm eq)}$. The peak of the normalized change in the differential energy density is located at $\epsilon \sim 5$, for both ν_e and ν_μ. Figure 6 of Ref. [11] also shows a peak at an $\epsilon \sim 5$. Although Fig. 2 shows that the deviation from equilibrium of the occupation probabilities increases for increasing ϵ-values, the probability is small enough in the high-ϵ bins that the large changes from equilibrium have little effect on the total energy density.

Integrating the neutrino energy distributions in Fig. 4, we find relative changes in the energy density of $\delta\rho_{\nu_e} = 0.0092$ and $\delta\rho_{\nu_\mu} = 0.0038$. The temperature ratio is given in the first row of Table II as $T_{\rm cm}/T = 0.7148$. Using Eq. (24),

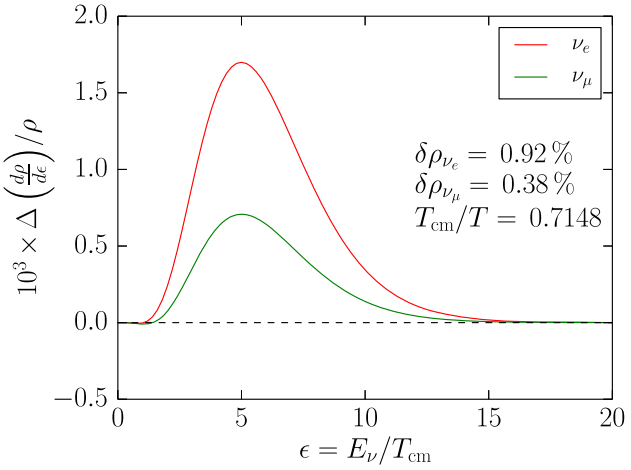

FIG. 4. The normalized change in the differential energy density [Eq. (29)] as a function of ϵ. The electron neutrinos exhibit a larger change compared to the muon neutrinos. The antineutrino evolution is nearly identical to the neutrino evolution for all flavors.

we find $\Delta N_{\rm eff} = 0.034$. The quantities $\delta\rho_{\nu_e}$, $\delta\rho_{\nu_\mu}$, $T_{\rm cm}/T$, and $N_{\rm eff}$ all agree closely with both Ref. [11] and DHS.

Figure 5 shows how the energy densities, $N_{\rm eff}$, and $T_{\rm cm}/T$ evolve with $T_{\rm cm}$ until they reach their asymptotic values. The $\delta\rho_{\nu_e}$ and $\delta\rho_{\nu_\mu}$ are computed from Eq. (21) and the relative change in $T_{\rm cm}/T$ is computed by comparing the evolution of the temperature with transport $(T_{\rm cm}/T)_{\rm all}$ and without $(T_{\rm cm}/T)_{\rm none}$:

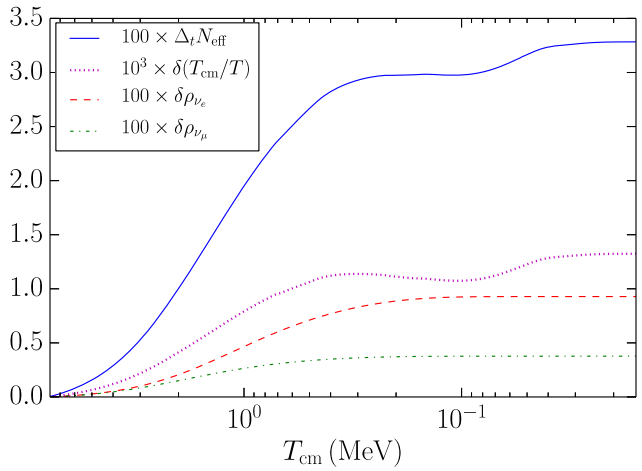

FIG. 5. Quantities related to energy density and temperature are plotted against the comoving temperature parameter. The blue solid curve shows the change in $N_{\rm eff}$ using Eq. (31). The red dashed curve shows the relative change in the energy density of ν_e. The green dash-dot curve shows the relative change in the energy density of ν_μ. The magenta dotted curve shows the relative change in $T_{\rm cm}/T$ using Eq. (30). At a given $T_{\rm cm}$, $\delta T_{\rm cm}/T > 0$ is equivalent to a lower plasma temperature in the transport case compared to no transport.

$$\delta(T_{\rm cm}/T) = \frac{(T_{\rm cm}/T)_{\rm all} - (T_{\rm cm}/T)_{\rm none}}{(T_{\rm cm}/T)_{\rm none}}. \tag{30}$$

Finally, to calculate the time evolution change in $N_{\rm eff}$, we use

$$\Delta_t N_{\rm eff} \equiv [1 + \delta(T_{\rm cm}/T)]^4 \times [(1 + \delta\rho_{\nu_e}) + 2(1 + \delta\rho_{\nu_\mu})] - 3, \tag{31}$$

where the subscript t denotes time dependence, in contrast to the asymptotic limit of Eq. (24). As may be seen in Fig. 5, $N_{\rm eff}$ does not converge to 3.034, the value consistent with DHS. The reason its asymptotic value is instead 3.033 is due to the fact that the run with no transport has $(T_{\rm cm}/T)_{\rm none} \neq (4/11)^{1/3}$ in the asymptotic limit. If we assume the neutrinos are in thermal equilibrium for $T > T_{\rm in}$, the temperature ratio incurs a modification from the finite electron rest mass as

$$\left(\frac{T_{\rm cm}}{T}\right)_{\rm none} = \left(\frac{4}{11}\right)^{1/3}\left(1 + \frac{5}{22\pi^2}z^2\right), \tag{32}$$

to second order in $z \equiv m_e/T_{\rm in}$. Setting $T_{\rm in} = 8$ MeV, we find an altered $T_{\rm cm}/T$ gives $\Delta N_{\rm eff} = 0.001$.

The evolution of $\delta(T_{\rm cm}/T)$ in Fig. 5 displays interesting features that are driven by the specifics of the loss of entropy in the plasma from the annihilation of electrons and positrons to neutrinos and the transfer of entropy from electrons/positrons to photons through annihilation (see Sec. IV for a detailed discussion of entropy). The annihilation of electrons and positrons into neutrinos can be seen in the rise of the $\delta\rho_\nu$ curves in Fig. 5. For $T_{\rm cm} \gtrsim 200$ keV, entropy is lost from the plasma into the neutrino seas resulting in a lower plasma temperature for the transport case (where entropy is lost) versus the no-transport case (where entropy is not lost). The increase in $\delta(T_{\rm cm}/T)$ for $T_{\rm cm} \gtrsim 400$ keV is caused by this entropy loss.

To analyze the entropy transfer from the electron/positron components to the photons, we need the total number densities of electrons and positrons

$$n_{e^\pm}(T, \mp\mu) = 2\int \frac{d^3p}{(2\pi)^3} f_{e^\pm}(E, T, \mp\mu), \tag{33}$$

which, in local thermodynamic equilibrium, are solely functions of the plasma temperature and the electron chemical potential. Figure 5 shows a different phasing of scale factor and temperature for the two cases. At a given $T_{\rm cm}$, the plasma temperature is always lower in the transport case versus the no-transport case.

Using a notation similar to that of Eq. (30), we define the absolute change in the number density of charged leptons as

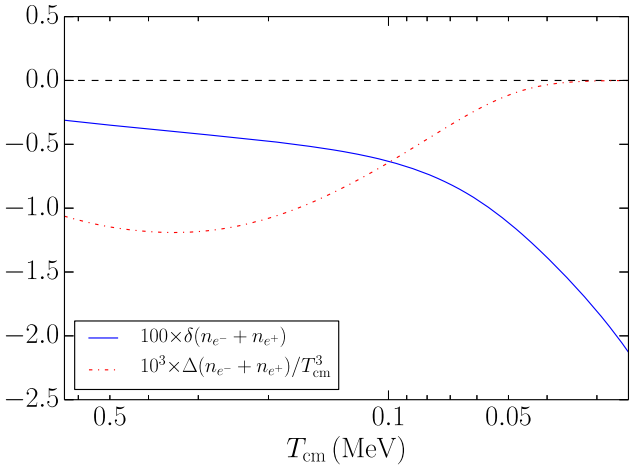

FIG. 6. Quantities related to charged lepton number density are plotted against the comoving temperature parameter. The blue solid curve is the relative change in the sum of positron and electron number densities as calculated in Eq. (35). The red dash-dot curve is the absolute change in the sum of positron and electron number densities, divided by $T_{\rm cm}^3$.

$$\Delta(n_{e^-}+n_{e^+}) \equiv (n_{e^-}+n_{e^+})_{\rm all} - (n_{e^-}+n_{e^+})_{\rm none}, \quad (34)$$

and the relative change in the number as

$$\delta(n_{e^-}+n_{e^+}) \equiv \frac{\Delta(n_{e^-}+n_{e^+})}{(n_{e^-}+n_{e^+})_{\rm none}}. \quad (35)$$

The quantity $(n_{e^-}+n_{e^+})/T_{\rm cm}^3$ is proportional to the total number of electrons and positrons in a comoving volume. The dot-dashed curve in Fig. 6 shows this quantity, while the solid curve in Fig. 6 shows the relative change in the number of charged leptons. The absolute change in the total number of charged leptons in a comoving volume is negative. This implies that there are fewer charged leptons and hence a lower plasma temperature in the transport case than in the no-transport case at a given $T_{\rm cm}$. The slope of the absolute change represents the different annihilation rates. The negative slope (at $T_{\rm cm} \gtrsim 400$ keV) indicates that the annihilation rate is greater in the transport case than in no-transport, while the opposite is true for $T_{\rm cm} \lesssim 400$ keV.

The rate at which entropy is transferred from the electrons and positrons to the photons is proportional to the annihilation rate divided by the plasma temperature. For 100 keV $\lesssim T_{\rm cm} \lesssim$ 400 keV, the competition between a larger annihilation rate in the no-transport case and the lower plasma temperature in the transport case results in a slight decrease in $\delta(T_{\rm cm}/T)$. Finally for $T_{\rm cm} \lesssim 100$ keV, the greater annihilation rate in no-transport results in an increasing $\delta(T_{\rm cm}/T)$ until virtually no electrons and positrons remain and $\delta(T_{\rm cm}/T)$ reaches its asymptotic value.

We turn now to the study of the individual and joint contributions of the annihilation and elastic processes.

B. Neutrino energy transport analysis

We return to the discussion of the weak interaction processes in Table I and their effect on neutrino observables that probe the changes to their energy density—the comoving-plasma temperature ratio, energy density changes, and $\Delta N_{\rm eff}$. The component contributions are collected in the following subsections in terms of the annihilation and elastic channels.

1. Annihilation channel

We focus here on annihilation-channel effects, which for the present purposes are defined according to Table I as processes $r = 10$ and 11. Figure 7 shows the relative changes in the occupation probabilities for the annihilation channels as a function of ϵ. The solid curves are when all weak interaction transport processes are neglected, except for annihilation of a neutrino and antineutrino into an electron-positron pair. The dashed curves are the same as the solid curves with the addition of processes $r = 1$ and 2. The dotted curves further include processes $r = 3$, 4 and 5. These processes do not exchange population among individual ϵ-values for a given flavor. Instead, there is an equilibration between the ν_e and ν_μ flavors. This is clearly seen in the figure since the difference between the dashed and dotted curves decreases relative to the solid, annihilation curves.

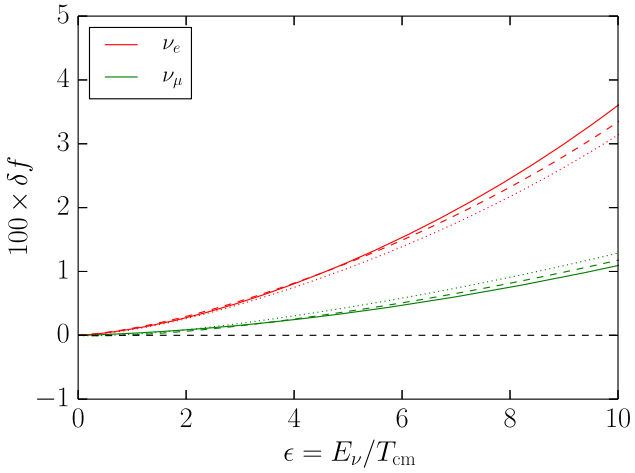

FIG. 7. The change in the neutrino occupation probabilities relative to the equilibrium distributions as a function of ϵ. Electron neutrinos exhibit a larger change compared to the muon neutrinos. Solid lines correspond to processes $r = 10$ and 11. Dashed lines correspond to processes $r = 1$, 2, 10 and 11. Dotted lines correspond to processes $r = 1, \ldots, 5$, 10 and 11.

2. Elastic scattering channel

Figure 8 shows changes relative to equilibrium for the combinations of processes involving elastic scattering of neutrinos on the charged leptons. It is distinguished by its behavior at low ϵ, where the change relative to equilibrium goes negative for $\epsilon \lesssim 4$, a feature not found in Fig. 7. Neutrinos, whose number are conserved in processes $r = 6, \ldots, 9$, upscatter and populate the larger epsilon bins. $N_{\rm eff}$ increases, and conversely, the energy in the plasma decreases. Processes $1, \ldots, 5$ behave much the same way as they do for the annihilation combinations. These processes act to equilibrate the occupation probabilities among flavors for a given bin. Perhaps surprisingly, the five neutrino-only processes do not appear to equilibrate the bins for a given flavor; the addition of the processes in rows $r = 1, 2$ do not change the intersection with the horizontal axis at $\epsilon \simeq 4$. The further additions of the processes in rows $r = 3, 4, 5$ also preserve the intersection point with the horizontal axis. Note that in both Figs. 7 and 8 there is a larger divergence between the solid, dashed, and dotted lines with increasing ϵ-value for the ν_e as compared to the ν_μ. This is because the population is transferred from ν_e into *both* ν_μ and ν_τ.

When adding the annihilation and elastic scattering channels together, as in Fig. 2, the annihilation channels are able to repopulate the low ϵ-values states. Annihilation erases much of the deficit caused by elastic scattering, although Fig. 2 shows that annihilation cannot entirely erase the deficit for $\epsilon \lesssim 1$.

C. Finite temperature QED radiative corrections

Our calculations show a new sensitivity to finite temperature QED radiative corrections. The feedback between neutrino energy transport and plasma conditions is especially sensitive to electron-positron pair number density as these are key targets for neutrino scattering. Previous works [1,2,10,44] include the effects of finite temperature QED radiative corrections. The corrections have been calculated for the electron mass and wave function renormalization, the electron-photon vertex and infrared photon emission and absorption. These corrections have an effect on a variety of quantities including the dispersion relation of the electron mass, weak interaction rates, and the equation of state.

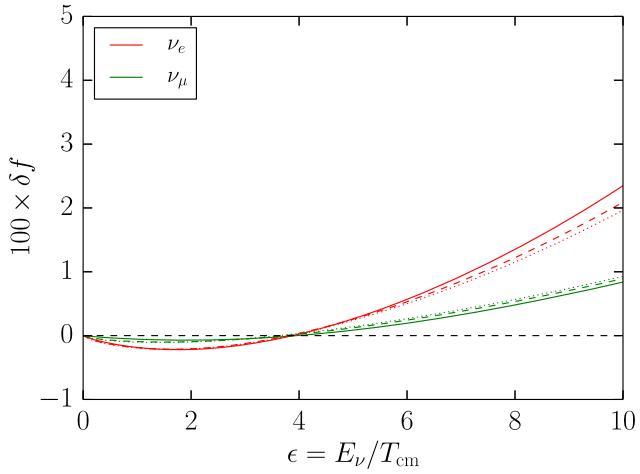

FIG. 8. The change in the neutrino occupation probabilities relative to the equilibrium distributions as a function of ϵ. The electron neutrinos again exhibit larger changes relative to the muon neutrinos. Solid lines correspond to processes $6, \ldots, 9$. Dashed lines correspond to processes $1, 2, 6, \ldots, 9$. Dotted lines correspond to processes $r = 1, \ldots, 9$.

In the present study, we include radiative corrections to the self-interaction energy for electrons, positrons, and photon dispersion relations. We follow the approach employed in Ref. [12]. This formulation is adopted primarily for comparison with previous results. We note, however, that the feedback between neutrino energy distribution evolution and plasma conditions can depend sensitively on the electron-positron pair density and that, in turn, can depend on these corrections. This highlights the need for a more complete treatment of finite temperature plasma effects. In any case, finite temperature QED radiative corrections by themselves have a small effect on, say, the relative ^{4}He abundance change, which is at the level of 10^{-4}, smaller than the neutrino transport effects that we are primarily concerned with in this work.

We apply finite temperature QED radiative corrections to contributions to the thermodynamic quantities ρ, p, $d\rho/dT$, $d\rho/d\phi_e$, $d(n_{e^-} - n_{e^+})/dT$, and $d(n_{e^-} - n_{e^+})/d\phi_e$. For the collision integrals of Sec. II A, we take the vacuum value of electron rest mass. In a preview of Sec. V, the weak interaction terms involving neutrinos and free nucleons utilize the electron rest mass at its vacuum value and do not include the higher-order effects detailed in Refs. [1,2,10]. Our $n \leftrightarrow p$ rates do not take into account the renormalization of the electron rest mass in any BBN computations. We have computed the effects of nonzero electron degeneracy $\phi_e \neq 0$ and found them to be negligible, so we take $\phi_e = 0$ in these radiative corrections. We maintain $\phi_e \neq 0$ in calculations of neutrino transport, weak rates, and overall charge neutrality with baryons.

Following Refs. [12,44] we take the shift in the electron rest mass δm_e to be

$$\delta m_e^2(p,T) = \frac{2\pi\alpha T^2}{3} + \frac{4\alpha}{\pi}\int_0^\infty dk \frac{k^2}{E_k}\frac{1}{e^{E_k/T}+1} - \frac{2m_e^2\alpha}{\pi p}\int_0^\infty dk \frac{k}{E_k}\log\left|\frac{p+k}{p-k}\right|\frac{1}{e^{E_k/T}+1}, \tag{36}$$

where $\alpha = e^2/(4\pi)$, $E_k = \sqrt{k^2 + m_e^2}$, T is again the plasma temperature. To be consistent with the procedure adopted in Ref. [12], we ignore the last, momentum p dependent term. According to Appendix B of Ref. [44] this

relation is valid for $T \ll m_e$. We note that the range of temperatures relevant for BBN include temperatures which do not satisfy this condition. It is nevertheless applied in the interest of comparison with previous results. Likewise for comparison purposes, the change in the photon mass [45] is taken as

$$\delta m_\gamma^2 = \frac{8\alpha}{\pi}\int_0^\infty dk \frac{k^2}{E_k}\frac{1}{e^{E_k/T}+1}. \tag{37}$$

We compute radiative corrections to the thermodynamic quantities by numerical integration of appropriately weighted distribution functions, including the dispersion relations with terms $\delta m_e(T)$ and $\delta m_\gamma(T)$. By contrast, Ref. [12] applies these same corrections but with a perturbative approach to the calculation of the thermodynamic quantities. Consequently, we obtain different asymptotic values for certain cosmological quantities from Ref. [12]. To wit, without the inclusion of neutrino transport, we obtain a value of $T_{\rm cm}/T = 0.7150$, implying $N_{\rm eff} = 3.020$. In the presence of neutrino transport, our values for the relevant neutrino parameters are

$$T_{\rm cm}/T = 0.7159, \tag{38}$$

$$\delta\rho_{\nu_e} = 8.908 \times 10^{-3}, \tag{39}$$

$$\delta\rho_{\nu_\mu} = 3.537 \times 10^{-3}, \tag{40}$$

$$N_{\rm eff} = 3.052. \tag{41}$$

Reference [13] employed a binned spectrum to investigate neutrino oscillations. The authors included the QED effects and found $N_{\rm eff} = 3.046$. Our value of $N_{\rm eff}$ is reasonably close, although it does differ from Ref. [13] by ∼12%. This difference may be due to differing methods of numerical evaluation. We are primarily concerned with changes in the primordial abundances relative to our baseline values which stem from self-consistent neutrino transport/BBN effects. Note that these transport-induced changes are an order of magnitude larger than the QED finite-temperature effects. Future work will focus on these subdominant contributions.

IV. ENTROPY TRANSFER AND GENERATION

The textbook treatment [22–24] of entropy exchange in the early universe takes into account entropy flow among the various components of the cosmic fluid but assumes that entropy generation is negligible. According to the Boltzmann H theorem, however, entropy increases whenever nonequilibrium kinetics obtain. Homogeneity and isotropy of the Friedmann-Lemaître-Robertson-Walker metric preclude a spacelike heat flow. The entropy in a comoving volume can change, however, if there is a timelike heat flow which respects the overall symmetry of homogeneity and isotropy on any spacelike surface $t =$ constant.

Of course, the weak decoupling of neutrinos from the plasma prior to and during BBN is a classic example of a nonequilibrium process and we therefore expect the total entropy to increase with increasing time/scale factor or decreasing comoving temperature. We have calculated the total entropy of the neutrino plus other plasma constituents in the early universe and find that it varies at the subpercent level. Nevertheless, there are entropy flows between the photon/electron/positron plasma and the decoupling neutrinos which are considerably larger than this and which alter nucleosynthesis relative to a no-transport case.

The entropy may be calculated generally—in either equilibrium or nonequilibrium states—as

$$S_i = -\int \frac{d^3x d^3p}{(2\pi)^3}[f_i \ln f_i + (1-f_i)\ln(1-f_i)], \tag{42}$$

for a species i. For species in equilibrium the above reduces to the familiar thermodynamic relation for the entropy per baryon s:

$$s \equiv \frac{S}{n_b V} = \frac{1}{n_b}\frac{\rho + P - \sum_i \mu_i n_i}{T}, \tag{43}$$

for baryon number density, n_b, energy density ρ, pressure P, chemical potential μ_i and number density n_i for species i.

Assuming homogeneity and isotropy, Eq. (42) leads to the entropy per baryon for general, nonequilibrium, states:

$$s_i = -\frac{T_{\rm cm}^3}{2\pi^2 n_b}\int_0^\infty d\epsilon \epsilon^2 [f_i \ln f_i + (1-f_i)\ln(1-f_i)], \tag{44}$$

where the occupation probabilities f_i are taken to be functions of ϵ and time. As described earlier, $T_{\rm cm}$ in Eq. (44) is a proxy for inverse scale factor, $a^{-1}(t)$. Since the comoving baryon number $n_b a^3$ is covariantly conserved, we have

$$\frac{T_{\rm cm}^3}{n_b} = \text{const.} \tag{45}$$

Taking the time derivative of Eq. (44), we determine the change in the entropy of species i by using the Boltzmann equation and general collision integral, $C_i[f_j]$,

$$\frac{ds_i}{dt} = -\frac{T_{\rm cm}^3}{2\pi^2 n_b}\int_0^\infty d\epsilon \epsilon^2 C_i[f_j]\ln\left(\frac{f_i}{1-f_i}\right). \tag{46}$$

The Boltzmann H theorem implies that the sum of the constituent entropies must be non-negative but the derivative of a given species, of course, has arbitrary sign.

We write the total entropy change in the neutrino sector as a summation over the individual species:

$$\frac{ds_\nu}{dt} = -\frac{T_{\rm cm}^3}{2\pi^2 n_b}\sum_{i=1}^{6}\int_0^\infty d\epsilon\epsilon^2 C_{\nu_i}[f_j]\ln\left(\frac{f_{\nu_i}}{1-f_{\nu_i}}\right). \quad (47)$$

Assuming equilibrium distributions for photons, electrons, and positrons, and ignoring the negligible contribution from baryons, we compute the change in entropy of the plasma employing equilibrium thermodynamics, taking account of energy conservation. We assume that cooling of the plasma occurs only due to interactions between neutrinos and charged leptons in scattering and annihilation processes. Heating due to nucleosynthesis, primarily from the release of binding energy of ^{4}He, is neglected since the relative contribution of the binding energy heat to the plasma is $\sim 10^{-9}$. This gives the change in entropy of the plasma due to heating of the neutrinos:

$$\frac{ds_{\rm pl}}{dt} = \frac{1}{n_b T}\frac{dq}{dt} = -\frac{T_{\rm cm}^4}{2\pi^2 n_b T}\sum_{i=1}^{6}\int_0^\infty d\epsilon\epsilon^3 C_{\nu_i}[f_j], \quad (48)$$

where q is the energy flux per unit volume and the sum is over neutrinos ν_i. The minus sign is required to define heat flow $q > 0$ out of the plasma. The time derivative of the total entropy per baryon is the sum of Eqs. (47) and (48):

$$\frac{ds_{\rm tot}}{dt} = -\frac{T_{\rm cm}^3}{2\pi^2 n_b}\sum_{i=1}^{6}\int_0^\infty d\epsilon\epsilon^2 C_{\nu_i}[f_j] \times\left[\epsilon\frac{T_{\rm cm}}{T} + \ln\left(\frac{f_i}{1-f_i}\right)\right], \quad (49)$$

which must be positive to satisfy the H theorem [46].

We show the change in the entropy-per-baryon components in Fig. 9. The blue curve of the top panel shows the entropy per baryon of the plasma as a function of comoving temperature. As expected, the plasma loses entropy as it heats and decouples from the neutrinos. The green curve of the middle panel gives the entropy per baryon in the neutrino seas as a function of comoving temperature. It is increasing due to heating from the plasma, also as expected. The red curve in the lower panel is the sum of $s_{\rm pl}$ and s_ν. As expected, it is a monotonically increasing function of time. We discuss the role of the entropy flows as shown in Fig. 9 in more detail below.

The lower panel of Fig. 9 shows that the epoch of weak decoupling occurs over $\sim 10^3$ Hubble times. Starting at the left side of the figure at $T_{\rm cm} = 8$ MeV we see that entropy[3] is already being exchanged between the plasma and the neutrinos, although at a low rate. Until the comoving temperature reaches about 2 MeV, this entropy exchange between the components of the cosmic fluid occurs *in equilibrium* since the total entropy (bottom panel) is constant. Near 1 MeV, the total entropy begins to deviate from its high-temperature, equilibrium value. In the region of temperatures from 8 MeV $> T_{\rm cm} >$ 2 MeV, the rates of *equilibrium* entropy exchange are increasing. The component entropies (top and middle panels), near $T_{\rm cm} \approx 1$ MeV, reach a point of inflection and, concomitantly, the total entropy begins to increase, deviating significantly from its high-temperature (low) value. More than half of the entropy transferred to the neutrinos from the plasma is complete by this temperature. As the comoving temperature continues to drop, going below 1 MeV, heating becomes more effective at changing the total entropy. During this epoch of *entropy*

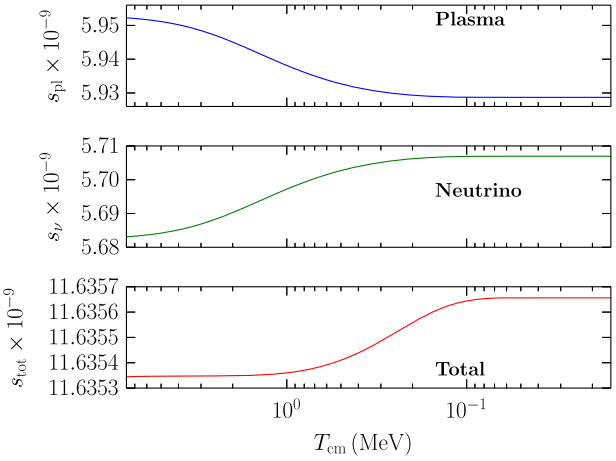

FIG. 9. The entropy per baryon for three sectors as functions of comoving temperature. The top panel (blue line) is the evolution of the entropy per baryon in the plasma, $s_{\rm pl}$. The middle panel (green line) is the evolution of the entropy per baryon in the neutrino sector, s_ν. The lower panel (red line) is the evolution of the total entropy per baryon, $s_{\rm tot}$.

TABLE III. Process-dependent changes in the plasma entropy. For all runs $\epsilon_{\rm max} = 20.0$, $N_{\rm bins} = 100$, $T_{\rm in} = 8$ MeV, $T_{\rm stop} = 15$ keV, $\varepsilon({\rm net/FRS}) = 30.0$. Column one gives the processes used for a given run similar to Table II. The second column is the initial entropy per baryon in the plasma at $T_{\rm in}$. Column three is final $s_{\rm pl}$ at $T_{\rm stop}$. Column four is the relative change between columns two and three.

Processes	$10^{-9}\times s_{\rm pl}^{(i)}$	$10^{-9}\times s_{\rm pl}^{(f)}$	$(s_{\rm pl}^{(i)} - s_{\rm pl}^{(f)})/s_{\rm pl}^{(f)}$
None	5.929	5.929	0
All	5.952	5.929	3.977×10^{-3}
10, 11	5.950	5.929	3.574×10^{-3}
1, 2, 10, 11	5.950	5.929	3.574×10^{-3}
1, 2, 3, 4, 5, 10, 11	5.950	5.928	3.663×10^{-3}
6, 7, 8, 9	5.933	5.929	7.426×10^{-4}
1, 2, 6, 7, 8, 9	5.933	5.928	7.798×10^{-4}
1, 2, 3, 4, 5, 6, 7, 8, 9	5.933	5.928	7.798×10^{-4}

[3]We refer to "entropy" from here on, though it is to be understood that this is the entropy per baryon.

production, the entropy generated by weak-interaction driven kinetic processes is larger than the entropy lost from the neutrinos. We note that, contrary to the order-of-magnitude estimates of Eq. (6), the process of weak decoupling, measured as the point at which the derivatives drop below some near-zero value, lasts until $T_{\rm cm} \simeq 90$–100 keV, well into the epoch of BBN.

Table III shows the initial, final, and relative changes in the entropy for the same runs as those performed in Sec. II. The first row ("None"), corresponds to the "standard" cosmology without transport. The second row ("All") corresponds to the curves in Fig. 9. Component contributions to the collision integrals, corresponding to various r in Table I, are given in the remaining rows. Here it is apparent that the dominant process contributing to entropy generation are due to the annihilation processes $r = 10$ and 11.

V. WEAK FREEZE-OUT AND NUCLEOSYNTHESIS

In this section we examine how the charged current weak reactions involving nucleons and the strong and electromagnetic nuclear reactions are affected by the evolving neutrino and plasma components. As outlined above, the scattering-driven nonequilibrium evolution of the neutrino energy distribution functions through the weak decoupling epoch is nonlinearly coupled to the plasma thermodynamic conditions. The plasma of photons, electrons, and positrons is maintained in thermal equilibrium by electromagnetic interactions whose rates are much faster than the Hubble rate for all epochs under present consideration. The rapid fall off in the weak interactions of neutrinos with neutrons and protons, however, result in the weak freeze-out of the n/p ratio where chemical equilibrium is no longer maintained even though thermal equilibrium still obtains. Systems where equilibrium is maintained instantaneously are, at any given time, insensitive to the previous history of the system. Quantities characterizing systems which are out of equilibrium, on the other hand, *can be sensitive* to previous history. In fact, since the n/p ratio and nuclear reactions are not in chemical equilibrium, the out-of-equilibrium neutrino energy distributions alter BBN abundance yields over the no-transport case.

As discussed in Appendix A, DHS (Ref. [7]) has taken into account effects of neutrino transport during weak decoupling on energy density, the weak interactions and the plasma temperature derivative. The work of DHS, which is most similar to our present treatment, however, employs a perturbative approach for nucleosynthesis. There, the primordial nucleosynthesis was "postprocessed" by using the results from DHS's prior solution of the coupled set of neutrino Boltzmann equations. Our treatment concurrently solves the Boltzmann equations for the neutrino occupation probabilities and the light nuclide abundances or mass fractions, given by

$$Y_i \equiv \frac{n_i}{n_b} \quad \text{and} \quad X_i \equiv A_i Y_i, \tag{50}$$

where for a given species i: n_i is the number density, A_i is the atomic mass number, Y_i is the abundance, and X_i is the mass fraction. The quantity n_b is the baryon number density. This fully coupled, self-consistent approach results in a significant enhancement of effects that change the light element abundances from the treatments without transport or with transport included perturbatively, as we detail in this section.

In both our transport and no-transport BBN calculations we employ the value of the baryon-to-photon ratio from Ref. [47], corresponding to $\omega_b = \Omega_b h^2 = 0.022068$. This also corresponds to the final entropy per baryon in the plasma of $s_{\rm pl} = 5.929 \times 10^9$ units of Boltzmann's constant. We emphasize that these are the *final* values of these quantities after all transport and entropy generating reactions have ceased, i.e., as measured at the CMB decoupling epoch. A standard BBN, baseline calculation assuming constant comoving entropy, but not including QED and other corrections, yields the following values for the primordial mass fraction of ^{4}He, relative abundances of deuterium, ^{3}He and ^{7}Li (with respect to hydrogen):

$$Y_P^{(\rm N)} \equiv X_{^4\rm He} = 0.2438, \tag{51}$$

$$({\rm D/H})^{(\rm N)} \equiv Y_{\rm D}/Y_{\rm H} = 2.627 \times 10^{-5}, \tag{52}$$

$$(^3{\rm He/H})^{(\rm N)} = 1.049 \times 10^{-5}, \tag{53}$$

$$(^7{\rm Li/H})^{(\rm N)} = 4.277 \times 10^{-10}. \tag{54}$$

We refer to the abundances in this baseline computation as (N). The standard BBN calculation and associated reaction network employed here is detailed in Refs. [36,39,48]. We emphasize that the (N) baseline computation does not include Coulomb corrections (CC), zero-temperature radiative corrections (0T), and transport-induced corrections (Trans). As an alternative baseline we consider the inclusion of Coulomb corrections (given by Eq. (5b) in Ref. [49]) to the reactions Eqs. (3) and (5) (on page 5); and zero-temperature radiative corrections (Eq. (2.14) in Ref. [1]) to reactions (3), (4), and (5). See Ref. [50] for a detailed discussion of the Coulomb corrections to BBN. The QED corrections discussed in Sec. III C are excluded for this baseline. The helium-4 (hereafter shortened to helium) mass fraction and relative abundances for this baseline are

$$Y_P^{(\rm Q)} = 0.2478, \tag{55}$$

$$({\rm D/H})^{(\rm Q)} = 2.650 \times 10^{-5}, \tag{56}$$

$$(^3{\rm He/H})^{(\rm Q)} = 1.052 \times 10^{-5}, \tag{57}$$

$$(^7\mathrm{Li/H})^{(\mathrm{Q})} = 4.317 \times 10^{-10}. \quad (58)$$

We refer to the abundances in this baseline computation as (Q). The (Q) baseline allows us to compare to other nucleosynthesis codes. To wit, in the (Q) baseline we obtain for the primordial helium mass fraction $Y_P = 0.2478$, which is within ~0.1% of the value from the PARTHENOPE code [51] of 0.24725 [52]. Table V shows the effect on the abundances for these cases.

We use a semi-implicit Heun's method to integrate the BBN nuclear reaction network [53] from $t = t_n$ to $t = t_{n+1}$. To calculate the abundance derivatives we need the abundance values themselves, Y_j, and a set of thermodynamic/transport quantities, namely T, T_{cm}, ϕ_e, ρ_b, and the ν_e, $\bar{\nu}_e$ occupation probabilities. We integrate the RK5 method by partitioning the time interval $\Delta t = t_{n+1} - t_n$ into six subintervals (see Ref. [43] for details on the fifth-order Runge-Kutta method with a Cash-Karp time step). We step through each subinterval and evolve the above set of thermodynamic/transport quantities (and other quantities as well) but not the Y_j. We extrapolate the small nucleosynthesis contributions to the derivative of ϕ_e (from alterations of the n/p ratio) and to the plasma-temperature derivative (from the release of nuclear binding energy and the n/p ratio) for each of the subintervals in the RK5 method. The baryon-to-photon ratio is small enough that the extrapolation does not produce substantial error in either the gross thermodynamics of the plasma or the Boltzmann neutrino-energy transport network (see Sec. IV). We store within memory the set of thermodynamic/transport quantities needed for the reaction network at two specific subintervals while integrating the RK5 method: the first subinterval (corresponding to the start of the time interval, $t = t_n$); and the fifth subinterval (corresponding to the end of the time interval, $t = t_n + \Delta t$). Once the RK5 terminates, we check for numerical convergence. If the convergence criteria failed, we repeat the RK5 calculation (beginning at $t = t_n$) with a smaller time step. If the convergence criteria succeeded, we accept the thermodynamic/transport quantities at $t_n + \Delta t = t_{n+1}$ and proceed to integrate the nuclear reaction network with Heun's method to obtain only the Y_j at t_{n+1}. Heun's method requires an initial evaluation at the start of the interval and a second evaluation at the end of the interval. We recall the set of thermodynamic/transport quantities stored in memory to use in the integration of the nuclear reaction network. Specifically, for the first computation we recall $T(t_n)$, $T_{\mathrm{cm}}(t_n)$, $\phi_e(t_n)$, $\rho_b(t_n)$, $f_{\nu_e}(\epsilon, t_n)$, $f_{\bar{\nu}_e}(\epsilon, t_n)$, and the *current* values of the abundances $Y_j(t_n)$ to calculate a first set of abundance derivatives. This is accomplished by utilizing the Jacobian of a linearized Boltzmann equation for nuclear reactions and subsequently diagonalizing a matrix (see Refs. [36] and [53] for details on this procedure). Using the time step value Δt and the first set of abundance derivatives, we estimate the new values of the abundances, $\tilde{Y}_j(t_n + \Delta t)$. At this stage in Heun's method, the $\tilde{Y}_j(t_n + \Delta t)$ are only *estimates* of the abundances at $t_n + \Delta t$; they are not the calculated abundances, i.e., the $Y_j(t_{n+1})$. Next, we calculate a second set of abundance derivatives again using the Jacobian of the linearized Boltzmann equation. This new set of derivatives requires the second set of thermodynamic/transport quantities, i.e., $T(t_{n+1})$, $T_{\mathrm{cm}}(t_{n+1})$, etc., and the previous estimates of the abundances, namely the $\tilde{Y}_j(t_n + \Delta t)$. Finally, we average the two sets of abundance derivatives and arrive at a derivative for each nuclide. We use this derivative and the time step to calculate the new value of the abundances $Y_j(t_{n+1})$. After we integrate the nuclear reaction network and have obtained the Y_j, we proceed to the next time point t_{n+1} and repeat the process.

With the two baseline calculations in hand, we are in a position to study the effect that weak interaction processes and neutrino transport has on the primordial abundances *relative to these baseline cases*. This comparison is done in Tables IV and V.

TABLE IV. Process-dependent changes in the BBN abundances. For all runs $\epsilon_{\max} = 20.0$, $N_{\mathrm{bins}} = 100$, $T_{\mathrm{in}} = 8$ MeV, $T_{\mathrm{stop}} = 15$ keV, $\varepsilon(\mathrm{net/FRS}) = 30.0$. The first column gives the processes used for a given run similar to Table II. Column two is the primordial mass fraction of ^{4}He and column three is the relative change from the (N) baseline case with no neutrino transport, i.e. the first row. Column four is the relative abundance of D and column five the relative change. Column six is the relative abundance of ^{3}He and column seven the relative change. Column eight is the relative abundance of ^{7}Li and column nine the relative change.

Processes	Y_P	δY_P	$10^5 \times \mathrm{D/H}$	$\delta(\mathrm{D/H})$	$10^5 \times {}^3\mathrm{He/H}$	$\delta({}^3\mathrm{He/H})$	$10^{10} \times {}^7\mathrm{Li/H}$	$\delta({}^7\mathrm{Li/H})$
None	0.2438	0	2.627	0	1.049	0	4.277	0
All	0.2440	4.636×10^{-4}	2.636	3.686×10^{-3}	1.050	1.209×10^{-3}	4.260	-3.916×10^{-3}
10, 11	0.2439	2.124×10^{-4}	2.635	3.202×10^{-3}	1.050	1.048×10^{-3}	4.262	-3.650×10^{-3}
1, 2, 10, 11	0.2439	1.515×10^{-4}	2.635	3.155×10^{-3}	1.050	1.032×10^{-3}	4.261	-3.672×10^{-3}
1, 2, 3, 4, 5, 10, 11	0.2439	2.415×10^{-4}	2.635	3.148×10^{-3}	1.050	1.029×10^{-3}	4.262	-3.543×10^{-3}
6, 7, 8, 9	0.2440	6.730×10^{-4}	2.629	1.002×10^{-3}	1.049	3.348×10^{-4}	4.276	-3.536×10^{-4}
1, 2, 6, 7, 8, 9	0.2440	5.455×10^{-4}	2.629	9.034×10^{-4}	1.049	3.001×10^{-4}	4.275	-3.972×10^{-4}
1, 2, 3, 4, 5, 6, 7, 8, 9	0.2440	5.533×10^{-4}	2.629	8.981×10^{-4}	1.049	2.981×10^{-4}	4.276	-3.797×10^{-4}

TABLE V. Changes in primordial abundances in BBN for Coulomb and radiative corrections. The first column gives the processes used for a given run. Rows correspond to various corrections as "CC" for Coulomb corrections; "0T" for zero-temperature radiative corrections; "Trans" for neutrino transport calculation with computational parameters as given in Table IV. The notation for the relative changes is the same as in Table IV. Row 4 is our (Q) baseline.

Processes	Y_P	δY_P	$10^5 \times \mathrm{D/H}$	$\delta(\mathrm{D/H})$	$10^5 \times {}^3\mathrm{He/H}$	$\delta({}^3\mathrm{He/H})$	$10^{10} \times {}^7\mathrm{Li/H}$	$\delta({}^7\mathrm{Li/H})$
None	0.2438	0	2.627	0	1.049	0	4.277	0
CC	0.2474	1.463×10^{-2}	2.647	7.898×10^{-3}	1.052	2.737×10^{-3}	4.317	9.344×10^{-3}
0T	0.2442	1.454×10^{-3}	2.629	7.816×10^{-4}	1.049	0.0	4.281	9.365×10^{-4}
CC, 0T	0.2478	1.613×10^{-2}	2.650	8.719×10^{-3}	1.052	3.021×10^{-3}	4.321	1.030×10^{-2}
Trans	0.2440	4.636×10^{-4}	2.636	3.686×10^{-3}	1.050	1.209×10^{-3}	4.260	-3.916×10^{-3}
CC, 0T, Trans	0.2479	1.644×10^{-2}	2.659	1.236×10^{-2}	1.053	4.209×10^{-3}	4.304	6.231×10^{-3}

In both Tables IV and V we show the change in a nuclide, δY, relative to the (N) baseline case as

$$\delta Y \equiv \frac{Y^{(\mathrm{proc})} - Y^{(\mathrm{N})}}{Y^{(\mathrm{N})}}, \tag{59}$$

where $Y^{(\mathrm{proc})}$ is the quantity of interest for the specific set of processes. $Y^{(\mathrm{N})}$ is the quantity of interest for the case of no transport and no higher-order corrections to the $n \leftrightarrow p$ rates. i.e. our (N) baseline value labeled "None" in row 1 of Tables IV and V.

Table IV gives the primordial mass fractions or relative abundances when various processes in Table I are included or neglected. This table shows that the transport calculations produce a 5×10^{-4} increase in the expected ^{4}He yield compared to $Y_P^{(\mathrm{N})}$. Table V gives corresponding changes between the (N) baseline case and the cases with Coulomb, zero-temperature radiative, or transport-induced corrections. We compare the helium yield in row 4 [the (Q) baseline] with the helium yield in the last row (labeled CC, 0T, Trans). The no-transport value in this baseline case is 0.2478, as mentioned above, while the same weak rate physics but with transport gives 0.2479, a roughly 3×10^{-4} increase in the helium yield. This is similar to the comparison above with the cases without Coulomb and zero-temperature radiative corrections, showing that the transport-induced alterations in light element abundance yields are somewhat robust to how this set of corrections to the $n \leftrightarrow p$ rates is treated. The increase in Y_P is in rough agreement with DHS irrespective of the baseline. Our hypothesis was that a high-energy enhancement of the ν_e occupation probability would lead to a smaller n/p ratio and subsequent decrease in Y_P. We have found the opposite behavior. Comparing the cases with and without transport, we find two competing processes affecting the helium abundance. With transport there is an enhanced population of ν_e and $\bar{\nu}_e$ relative to FD equilibrium, and this results in an enhanced neutron destruction in the channel $\nu_e + n \to p + e^-$. (The $\bar{\nu}_e + p \to n + e^+$ channel is hindered by a threshold energy.) A decrease in the neutron number leads to a decrease in helium. Second, a larger energy density in the neutrino sector yields a faster expansion rate, and this means a larger neutron number during weak freeze-out, which would produce a higher helium yield. Tables IV and V show that the net change in helium with these two effects is nearly a wash, with the faster expansion rate being the more dominant process and a very small increase in helium (0.2478 to 0.2479 in Table V).

We have investigated our theory by the following numerical test. We run our code with all of the neutrino transport processes activated to allow the neutrino occupation probabilities to go out of FD equilibrium. We follow the flow of entropy out of the plasma and calculate the Hubble expansion rate, but we do not use the modified occupation probabilities in calculating the neutron-to-proton rates. Instead, we simply use FD occupation probabilities when calculating the weak interaction rates. This program ensures that we have the same thermodynamics and phasing of T with T_{cm}, and therefore tests how effective the high-energy tail of the ν_e distribution is at lowering the helium abundance. The results of the test are a slight increase of helium to 0.2480, over the 0.2479 value in row 6 of table V. The increase in the ν_e occupation probability has a very slight overall leverage on the helium abundance. For this test, the changes in deuterium, helium-3, and lithium-7 are even smaller.

Neutrino transport alters the deuterium abundance computed from the baselines in a significant and interesting way. Table IV (second row) shows an increase of about 0.4% in the predicted BBN D/H value relative to the (N) baseline. Table V gives the corresponding changes relative to our (Q) baseline case, and again shows a comparable fractional increase in the deuterium yield. This is a change which is comparable to the level of BBN nuclear physics input uncertainties [i.e., in the $\mathrm{D}(p,\gamma)^3\mathrm{He}$ cross sections] [54] and these might be improved upon by *ab initio* many-body calculations [55]. Moreover, our calculated increase is not far from the speculated precision in the primordial D/H abundance attainable with thirty-meter-class telescopes and observations of isotope-shifted Lyman series hydrogen absorption lines in nearly pristine hydrogen clouds seen along lines of sight to high-redshift quasars [56–59].

Tables IV and V also show the changes in the lithium-7 yield with and without transport. The changes in this case

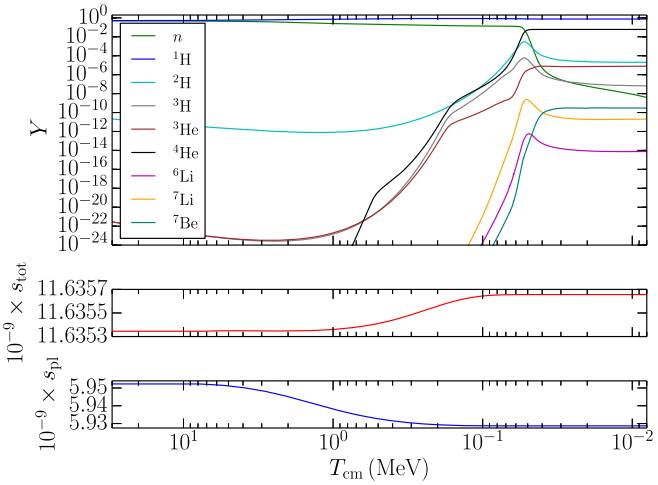

FIG. 10. Top panel: evolution of nuclear abundances as a function of comoving temperature parameter. Middle panel: evolution of the total entropy as a function of scale factor. Lower panel: evolution of entropy carried by the photon/electron/positron plasma. Coulomb and zero-temperature radiative corrections are not included in this plot.

are roughly 0.3% relative to either baseline calculation. This reduction is more than two orders of magnitude below that needed to address the factor of 3 or 4 overprediction of the primordial ^{7}Li abundance that constitutes the "lithium problem." It has been argued that there is no nuclear physics fix for this problem (see for example Refs. [38,60]). BSM physics, like out of equilibrium decays of massive particles (see Refs. [19,20,61]), or massive particle decay and post-BBN cascade nucleosynthesis [62] may be required if the observationally inferred lithium abundance is indeed primordial [63].

Figure 10 shows the transport-coupled BBN light element abundance histories as a function of decreasing $T_{\rm cm}$ or, equivalently, increasing time. Note that the entropy in the plasma $s_{\rm pl}$ is decreasing, as entropy flows into the decoupling neutrino seas, primarily in the early phases of BBN. This is during the epoch when many but not all nuclear species are maintained in NSE by relatively large nuclear reaction rates. In NSE the nuclear abundances are set by the n/p ratio, the nuclear binding energies, and the relevant entropy per baryon, namely $s_{\rm pl}$.

The nonlinear effect of neutrino transport on $N_{\rm eff}$, discussed in Sec. III, is also observed in the primordial abundances. It is associated with the change in the phasing of the time development of the entropy, plasma temperature, and n/p ratio relative to the no-transport, constant comoving entropy case. The transport-induced higher expansion rate implies that the plasma temperature will decrease at a more rapid rate after the alpha-particle-formation epoch ($T_{\rm cm} \sim 50$ keV in Fig. 10). After the majority of neutrons are isolated within alpha particles, deuterium begins to decrease until it freezes-out at $T_{\rm cm} \sim 20$ keV. There is less time for the temperature-sensitive deuterium destruction reactions to operate. At the deuterium peak (coincident with the alpha-particle formation epoch), the most effective deuterium destruction channels are the purely strong interactions, namely $^3{\rm He}(d,p)\alpha$ and $t(d,n)\alpha$, where we have used shorthand nuclear notation for deuterium (d), tritium (t), and ^{4}He (α). The former reaction is hindered relative to the latter because the former has a larger Coulomb barrier than the latter. This is evidenced by the parallel tracks of deuterium and tritium for 50 keV $> T_{\rm cm} >$ 20 keV. However, deuterium is also efficiently destroyed by the electromagnetic channels: $d(p,\gamma)^3{\rm He}$ and $d(\gamma,p)n$. In addition, the electromagnetic reactions are also sensitive to temperature. Note that the former reaction produces ^{3}He and there is a slight increase of ^{3}He on the lower temperature side of the deuterium peak. Due to the increased energy density from neutrino transport, both the strong and electromagnetic reactions have less time to destroy deuterium compared to the no-transport case. The result is a higher deuterium yield.

The neutrino transport calculations alter the neutrino energy distribution functions and thus the charged-current weak interaction histories for the n/p ratio, which change BBN abundance yields over those in Eqs. (51)–(54) and Eqs. (55)–(58). The most important charged-current processes at late times ($T_{\rm cm}\sim$ several hundred keV) are those without thresholds, i.e., $\nu_e + n \to p + e^-$ and $e^+ + n \to p + \bar{\nu}_e$ [50,64]. Helium is sensitive to n/p, which is altered by a competition between the effect of high-energy electron-flavor neutrinos that convert neutrons to protons and the effect of the increased energy density present in neutrinos and antineutrinos of all flavors that cause an increase in the cosmic expansion rate. The deuterium yield also appears to be sensitive to the freeze-out of the nuclear reactions due to the increased expansion rate.

Figure 11 shows a plot of how the electron fraction Y_e evolves with comoving temperature. Y_e is given in terms of

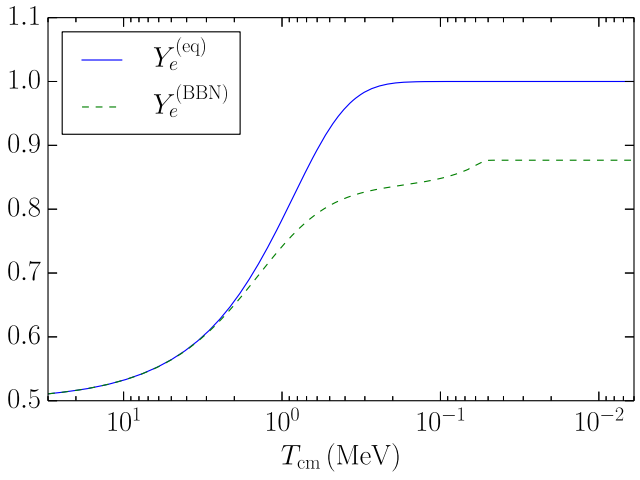

FIG. 11. Evolution of the electron fraction Y_e as a function of comoving temperature parameter $T_{\rm cm}$. Coulomb and zero-temperature radiative corrections are not included in this plot.

the n/p ratio by $Y_e = 1/(1+n/p)$. The evolution of the n/p ratio is given by

$$\frac{d}{dt}(n/p) = (1+n/p)(\lambda_p - \lambda_n n/p), \tag{60}$$

where λ_p and λ_n are the total weak charged-current proton and neutron destruction rates, respectively. Figure 11 gives the actual electron fraction, $Y_e^{(\mathrm{BBN})}$, determined from Eq. (60) with the transport-calculated neutrino energy distributions and the nuclear reaction network. In addition, Fig. 11 shows the electron fraction assuming weak equilibrium throughout the range of temperature considered

$$Y_e^{(\mathrm{eq})} = \frac{1}{1+e^{-\delta m_{np}/T+\phi_e-\xi_{\nu_e}}}, \tag{61}$$

where $\delta m_{np} \equiv m_n - m_p$, the differences of the neutron and proton rest masses, respectively, ϕ_e is the electron degeneracy, and ξ_{ν_e} is the $\nu_e/\bar{\nu}_e$ degeneracy parameter. In the equilibrium plot in Fig. 11, we take $\phi_e = \xi_{\nu_e} = 0$.

VI. CONCLUSION

We have performed a fully self-consistent, and simultaneous, calculation of the evolution of the neutrino energy distribution functions and all strong, electromagnetic and weak nuclear reactions during the epochs in the early universe where neutrinos decouple and primordial nuclear abundances are set. A key result of this calculation is to show that there is nonlinear feedback between the time/scale factor evolution of the neutrino sector and the corresponding evolution of the photon/electron/positron/baryon plasma. The neutrino energy transport part of this calculation yields essentially the same final result as previous treatments, at least in terms of final, post BBN, relic neutrino energy distributions, where the final entropy-per-baryon (or baryon-to-photon ratio) matches the value of this quantity as inferred from CMB measurements at the photon decoupling epoch. However, our calculation reveals that the history of, and phasing of the neutrino and plasma components, and associated entropy flow and generation, is altered when nonlinear feedback is included. Systems in instantaneous equilibrium are, of course, blind to the history of conditions and system parameters. This is not the case for nonequilibrium systems. Indeed, our calculations show that out-of-equilibrium components in the early universe can be sensitive to the history of how neutrino energy distributions and plasma thermodynamic conditions got to their final states. These nonequilibrium components include the entire weakly interacting system of neutrinos, electrons, positrons, neutrons, and protons, as well as important segments of the strong and electromagnetic nuclear reaction network. In fact, our calculations show changes in the BBN light element abundance yields relative to baseline BBN calculations with no neutrino energy transport. These changes stem, in part, from feedback between the nonequilibrium sectors. Appendix A gives an account of previous important work in this area which we have built on.

In Sec. II we describe in detail the new computational tool, BURST, that we developed to do the coupled, simultaneous modeling of all standard-model early universe components. We have tested the performance and accuracy of the code, as discussed in Sec. II B. Evaluation of integrals of the collision terms entering the Boltzmann equation assure the conservation of neutrino lepton number at the level of 1 part in 10^{14}. Efficient numerical methods have been developed for execution on parallel platforms. In Appendixes B and C we provide a detailed exposition of the neutrino scattering processes and corresponding kernels and integrals used in these parallel computations.

Section III details the results specific to the neutrino sector when the charged lepton, neutrino and photon components are evolved. Our calculations reveal a rich history of timelike entropy flow between the components of the early universe. If we use N_{eff} to parameterize the increase in the energy density of neutrinos, we find $N_{\mathrm{eff}} = 3.034$ when we include only transport processes, and $N_{\mathrm{eff}} = 3.052$ when we include transport and QED effects. Furthermore, we have uncovered a novel late-time rise in relativistic energy density ($\Delta_t N_{\mathrm{eff}}$, shown in Fig. 5) when the entropy in $e^{\pm}$ pairs is transferred to photons.

We have dissected the contributions of each neutrino scattering and reaction channel to distortions in neutrino energy spectra, along with the concomitant effects on the entropy flows. A key conclusion of our work is that the changes in cosmological quantities stemming from various processes do not add incoherently and must be followed in a full nonlinear, coupled treatment.

Our work may suggest a new way in which in-medium corrections to electron/positron rest masses and other plasma corrections are important. It is clear from our calculations that the timelike flow of entropy between the components in the early universe medium, the evolution of the neutron-to-proton ratio and nuclear abundances, and the phasing of these processes relative to scale factor and plasma temperature, must be adequately modeled if we hope to predict light element BBN abundance yields to better than $\sim$1% precision. The key processes facilitating entropy transfer, and determining the associated phasing, are those involving neutrino-electron/positron scattering/annihilation. Consequently, the number density history of $e^{\pm}$-pairs can be important. We presented calculations with and without neutrino energy transport, both of which included QED corrections to the thermodynamics of the plasma. From these calculations we can see that important aspects of entropy flow and neutron-to-proton evolution and phasing are being set at temperatures less than twice the electron rest mass. In this regime, the $e^{\pm}$-pair density can be nearly exponentially sensitive to the *in-medium* electron

rest mass. This suggests that finite temperature corrections take on a new importance in calculating neutrino transport and BBN.

Transport-induced changes in the $n \leftrightarrow p$ rates, as detailed in Sec. V, appear to be independent of the particular implementation of Coulomb [50] and zero-temperature radiative corrections. However, other effects on the $n \leftrightarrow p$ rates, such as finite-temperature radiative corrections, in-medium renormalization of the electron and positron rest masses, or inclusion of in-medium nucleon rest mass corrections and nuclear recoil [10] may indeed alter the primordial abundances in a nonlinear way when neutrino transport is included.

The transport collision-term calculations detailed in Sec. III are an incremental step in describing the neutrino evolution of the early universe. We do not include neutrino oscillations in this paper (see [13] for an analysis of this problem with neutrino oscillations). However, we plan to expand the current Boltzmann-solver code into a quantum-kinetic approach for handling neutrino flavor density matrices, i.e. along the lines of the QKEs in Ref. [25]. If the QKEs lead to an equilibration between ν_e and ν_μ (as highlighted in Figs. 1–4) we would expect a decrease in $N_{\rm eff}$ due to the lack of a charged-current diagram in the ν_μ scattering processes. The equilibration has two indirect effects on nucleosynthesis. A decrease in $N_{\rm eff}$ is equivalent to less radiation energy density which would imply a smaller Hubble expansion rate. The slower expansion rate delays weak freeze-out and would yield a smaller n/p (and smaller primordial helium abundance) compared to the case we explore here: energy transport without oscillations. In addition to modifying the energy density, neutrino oscillations will decrease the population of the ν_e, causing an earlier epoch of weak freeze-out and subsequent increase of n/p. It would appear, from our calculations in this paper, that Y_P is more sensitive to the change in expansion rate than the distortion of the ν_e spectrum. Furthermore, our best prediction of $N_{\rm eff}$ is $N_{\rm eff} = 3.052$, which is $\sim$0.01 larger than the Ref. [13] value of 3.046. The principal difference between our treatment and that of Ref. [13] is our exclusion of neutrino oscillations. The difference may be a signature of oscillations. However, the QKE problem is inherently nonlinear and requires a sophisticated calculation to verify quantitative and qualitative predictions.

We have demonstrated, in Sec. IV that the textbook treatment of neutrino weak decoupling from the plasma, which assumes covariant conservation of entropy, is largely satisfied. Small numerical deviations from comoving entropy conservation, as shown in Figs. 9, 10, and 12 have a significant and potentially measurable effect on the light primordial nuclide abundances at the level of $\sim$0.5%. We discussed the two regimes of *equilibrium* entropy exchange and entropy generation. Further, we have shown that the weak-decoupling and BBN epochs overlap in time significantly and suggest that they should be regarded as the single epoch termed the "weak-decoupling-nucleosynthesis" epoch.

As presented in Sec. V, the neutrino transport-altered history of weak decoupling and weak freeze-out results in potentially significant changes in predicted BBN abundance yields. As Table IV shows, these include an increase of 0.4% in the BBN-predicted D/H yield relative to baseline no-transport calculations. In addition, Table V shows the changes in the primordial light nuclide abundances when selections of radiative and Coulomb corrections are taken into account. These variations are similar in size to the uncertainties associated with observational uncertainties and those due to nuclear physics uncertainties. The anticipated precision of extremely large, thirty-meter-class telescopes will hopefully approach this precision within a decade.

Figure 12 shows the temperature range spanning the weak-decoupling, $e^\pm$ annihilation, weak freeze-out, and BBN epochs. The curve in the first panel is the evolution of the entropy in the photon/electron/positron/baryon plasma, $s_{\rm pl}$, with respect to $T_{\rm cm}$ and illuminates the physics of the weak-decoupling epoch. The curve in the second panel is the evolution of the temperature ratio $T_{\rm cm}/T$ with respect to $T_{\rm cm}$ through the $e^\pm$ annihilation epoch. The curve in the third panel is the electron fraction Y_e and shows the evolution of the weak freeze-out epoch. The last curve in the fourth panel is the relative abundance of deuterium D/H characteristic of the BBN epoch.

Our calculations show that careful, high precision modeling of the complicated, nonlinear interplay of

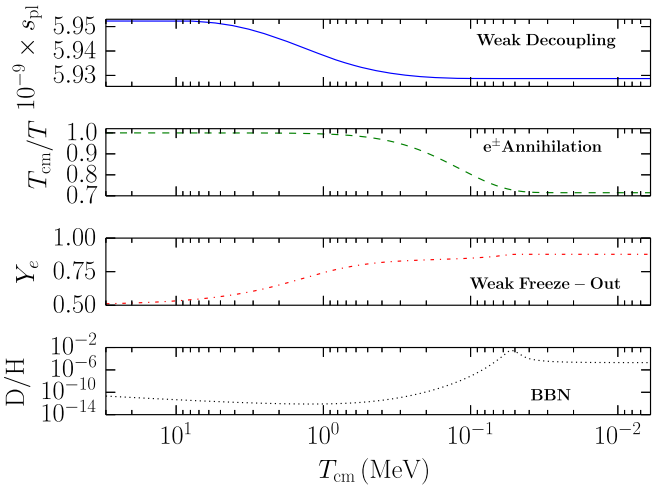

FIG. 12. The entropy, temperature ratio, electron fraction, and relative abundance of deuterium as functions of comoving temperature. The blue solid line is the evolution of the entropy per baryon, $s_{\rm pl}$, in the plasma as a function of comoving temperature, $T_{\rm cm}$. The green dashed line is the evolution of the ratio of comoving temperature to plasma temperature, $T_{\rm cm}/T$ as a function of $T_{\rm cm}$. The red dash-dot line is the evolution of the electron fraction, Y_e, as a function of $T_{\rm cm}$. The black dotted line is the evolution of the relative abundance of deuterium, D/H, as a function of $T_{\rm cm}$.

out-of-equilibrium constituents in the early universe is required if the goal is to predict BBN light element abundance yields and relic neutrino properties to better than one percent precision. In fact, the expected high precision data from Stage-IV CMB experiments and from thirty meter class telescopes sets up a unique opportunity to probe cosmology and BSM physics operating in the early universe [59]. Moreover, new laboratory data on neutrino properties, e.g., the neutrino mass hierarchy or neutrino rest mass constraints [65], may be forthcoming, and these may impact the evolution of the neutrino and nuclear components in the early universe. High-precision BBN/neutrino calculations likely will be an important cornerstone of this enterprise.

ACKNOWLEDGMENTS

We thank Fred Adams, Eve Armstrong, Kam Arnold, Daniel Blaschke, Lowell Brown, John Carlstrom, John Cherry, Vincenzo Cirigliano, Scott Dodelson, Lauren Gilbert, Luke Johns, Brian Keating, Lloyd Knox, Adrian Lee, Eric Michelsen, Ken Nollett, Amol Patwardhan, Shashank Shalgar, Meir Shimon, Gary Steigman, Mike Turner, and Nicole Vassh for useful conversations with respect to cosmology, neutrino physics, nuclear physics, plasma physics, Fortran 90, and parallel computing. This work was supported in part by NSF Grant No. PHY-1307372 at UC San Diego. This work was supported also by the Los Alamos National Laboratory Institute for Geophysics, Space Sciences and Signatures Subcontract No. 257842. This research used resources provided by the Los Alamos National Laboratory Institutional Computing Program, which is supported by the U.S. Department of Energy National Nuclear Security Administration under Contract No. DE-AC52-06NA25396. We thank the anonymous referee for their useful comments.

APPENDIX A: OVERVIEW OF PAST APPROACHES

The departure from equilibrium in weak decoupling and its subsequent effects on nucleosynthesis has been studied by many groups. Early work [1–4] considered the neutrinos to have a thermal distribution after weak decoupling and calculated the consequences of $e^{\pm}$ annihilation on the temperature of this thermal distribution. The focus of Refs. [1,2] was to examine the effect of finite-temperature radiative corrections to the neutron-proton conversion rates to study changes in helium production. The corrections change the neutrino spectra and thus increase the ratio $T_{\rm cm}/T$. References [3,4] treated the neutrinos and the electrons/positrons as two relativistic gases with different temperatures and calculated the relaxation time over which these two components of the universe would return toward thermal equilibrium.

Recent work has instead shifted toward solving the coupled Boltzmann equations, that deal directly with the neutrino distribution functions. One approach has been to treat neutrino scattering processes and neutrino production in electron-positron annihilation approximately, which treats the out-of-equilibrium effects as a perturbation on the FD spectrum of neutrinos. Reference [5] solves the Boltzmann equations using Maxwell-Boltzmann statistics, yielding both a perturbation in the neutrino temperature and a first-order perturbation to the FD neutrino spectrum. References [11,12] adopt a perturbative approach in introducing orthogonal polynomials that use the FD occupation probability as a weight function.

Other approaches (and the approach we employ in this work) discretize the neutrino distribution function on a comoving invariant momentum, $p/T_{\rm cm}$. The neutrino distribution function is binned, creating a coupled set of Boltzmann equations for the evolution of each bin to be solved numerically. These approaches do not use the Maxwell-Boltzmann statistics approximation used in past works (cf., Ref. [5]), instead using the full FD blocking factors in the collision integrals. Reference [6] introduced a general neutrino distribution function and showed values consistent to those in Ref. [5] when using the Maxwell-Boltzmann approximation. Reference [8] used a pseudo-logarithmic binning scheme and employed a unique numerical scheme which did not require the calculation of the full Jacobian matrix.

Reference [7] (DHS) uses 100 linearly spaced bins spanning $0 \le p/T_{\rm cm} \le 20$ (200 bins are also used, but acceptable convergence is found with 100 bins). In their seminal work, DHS runs a number of convergence tests and finds that the convergence of the results is most sensitive to the number of time steps (steps in scale factor) taken from a prescribed initial to final epoch as compared to number of bins, initial epoch, binned spectrum vs a perturbation function of the spectrum, or ODE evolution algorithm: simple (presumable Eulerian) time evolution vs Bulirsch-Stoer routine. An addendum [9] improved the accuracy of their code and found no change in the result, $N_{\rm eff} = 3.034$.

The above works focused on out-of-equilibrium processes that augment the neutrino seas relative to a scenario where there is a sharp decoupling of neutrinos from the plasma. Finite-temperature quantum electrodynamic (QED) radiative corrections provide $\mathcal{O}(\alpha)$ corrections to the dispersion relations of electrons, positrons and photons which, in turn, affect the entropy transferred to the photon-baryon plasma when the electrons and positrons annihilate. Reference [44] calculated the QED correction to the dispersion relation for electrons to first order in the fine-structure constant, α. Using the altered dispersion relation, Ref. [10] employed entropy conservation to find the corrections to the temperature ratio $T_{\rm cm}/T$. Reference [45] introduced a QED correction to the dispersion relation for photons, giving photons an effective nonzero mass. Reference [12] extended their method to perturbatively solve the Boltzmann equation

TABLE VI. Summary of previous work. For all works that do not explicitly report a value of $N_{\rm eff}$ (Refs. [1–6]), Eq. (22) or (23) is used to estimate a value of $N_{\rm eff}$ from parameters reported. For Ref. [6], we include two estimates of $N_{\rm eff}$: (1) the relative changes in energy density implicitly contain the change in temperature (3.017), and (2) the energy densities do not contain the change in temperature (3.027).

References	Notes	$N_{\rm eff}$
[1,2]	(a) (i) finite-temperature radiative corrects to neutron-to-proton rates (ii) average cross sections to estimate neutrino production during $e^{\pm}$ annihilation	3.020
[3,4]	(b) (i) relaxation-time formalism to calculate changes in neutrino temperature post-weak decoupling	3.024 [3] 3.022 [4]
[5]	(c) (i) coupled set of Boltzmann equations in weak decoupling (ii) Maxwell-Boltzmann statistics (iii) solves for a change in the neutrino temperature and a first-order change to the neutrino distribution functions	3.022
[11,12]	(d) (i) perturbative approach solving Boltzmann equations using a series of orthogonal polynomials to describe perturbations from a FD neutrino spectrum	3.035
[6]	(e) (i) coupled set of Boltzmann equations in weak decoupling using FD statistics (cf., Ref [5]) (ii) solves for a change in the neutrino temperature and a general neutrino distribution function	3.017 or 3.027
[8]	(f) (i) solves coupled Boltzmann equations by binning the neutrino distribution function (ii) pseudologarithmic binning scheme: 40 linearly spaced bins per decade ranging from $10^{-5.5} \leq p/T_{\rm cm} \leq 10^{1.7}$ (iii) employ unique numerical scheme that does not require calculation of the full Jacobian matrix—more efficient than standard adaptive RK5 scheme by a factor of 20–60	3.022
DHS [7,9]	(g) (i) solves coupled Boltzmann equations by binning the neutrino distribution function (ii) 100 linearly spaced bins between $0 \leq p/T_{\rm cm} \leq 20$ (iii) includes convergence studies regarding binning of neutrino spectrum and ODE solver	3.034
[10,44,45]	(h) (i) introduces QED corrections to electron and photon dispersion relations (ii) no Boltzmann evolution, just conservation of comoving entropy	3.011 [10]
[12]	(i) (i) includes QED corrections to the perturbative approach with orthogonal polynomials described above for Ref. [12]	3.0395
[14]	(j) (i) includes QED corrections to the perturbative approach with orthogonal polynomials (ii) assumes neutrino spectra in thermal equilibrium, but not necessarily in chemical equilibrium (iii) uses a different set of orthogonal polynomials as compared with Ref. [12]	3.044
[13]	(k) (i) includes QED corrections along with solving Boltzmann equations by binning the neutrino distribution function (ii) improved numerical technique as compared to Ref. [12]	3.046

while simultaneously including the QED corrections to the dispersion relations for positrons/electrons [44] and photons [45]. Reference [14] assumed that the neutrino spectra were close to thermal equilibrium, but need not be in chemical equilibrium, so they used orthogonal polynomials based on a weight function mirroring a FD spectrum with nonunit fugacity.

Lastly, Ref. [13] combined a linear binning of the neutrino distribution spectrum and the QED corrections to obtain $N_{\rm eff} = 3.046$, a result that is routinely cited in the literature. Another aspect of this work was the inclusion of neutrino oscillations, which changed the energy densities of the individual neutrino species, but did not overall change $N_{\rm eff}$. Table VI summarizes the approaches of past work in this area. While not all works cite a value of $N_{\rm eff}$, we use Eqs. (22) and (23) to translate from the published calculations to $N_{\rm eff}$.

APPENDIX B: NEUTRINO-NEUTRINO SCATTERING

This appendix details the reduction of the collision integral for neutrino-neutrino elastic scattering. We will make the approximation that neutrinos are massless for all three flavors. We start with the summed-squared amplitude for neutrinos scattering on other neutrinos with identical flavor (row 1 of Table I):

$$\nu(1) + \nu(2) \leftrightarrow \nu(3) + \nu(4), \tag{B1}$$

$$\langle |\mathcal{M}_1|^2 \rangle = 2^7 G_F^2 (P_1 \cdot P_2)(P_3 \cdot P_4). \tag{B2}$$

Conservation of four-momentum implies $P_1 \cdot P_2 = P_3 \cdot P_4$. The collision integral is [22]

$$I \equiv C_{\nu_1}[f_j] = \frac{1}{2p_1}\int \frac{d^3p_2}{(2\pi)^3 2p_2}\frac{d^3p_3}{(2\pi)^3 2p_3}\frac{d^3p_4}{(2\pi)^3 2p_4}(2\pi)^4\delta^{(4)}(P_1+P_2-P_3-P_4)2^7 S_1 G_F^2 (P_1\cdot P_2)^2 F(p_1,p_2,p_3,p_4). \tag{B3}$$

Using the three-momentum part of $\delta^{(4)}$, we eliminate the integral over d^3p_4:

$$I = \frac{1}{2p_1}\frac{(2\pi)^4 2^7 S_1 G_F^2}{2^3(2\pi)^9}\int \frac{d^3p_2}{p_2}(P_1\cdot P_2)^2 \int \frac{d^3p_3}{p_3 p_4}\delta(p_1+p_2-p_3-p_4)F(p_1,p_2,p_3,p_4)|_{p_4=|\mathbf{p}_1+\mathbf{p}_2-\mathbf{p}_3|}, \tag{B4}$$

where $\mathbf{p}_i$ is the three-momentum of the ith particle, and p_4 is no longer an integration variable, but instead related to the other integration and free variables through

$$p_4^2 = |\mathbf{p}_1+\mathbf{p}_2|^2 + p_3^2 - 2|\mathbf{p}_1+\mathbf{p}_2|p_3\cos\theta_3, \tag{B5}$$

where we have defined the integration variable θ_3 to be the angle between $\mathbf{p}_1+\mathbf{p}_2$ and $\mathbf{p}_3$. To simplify $\int d^3p_3$, we first consider $\int d\theta_3$ and use the following u substitution:

$$u^2 = p_4^2, \tag{B6}$$

$$\Rightarrow 2p_4 du = -2|\mathbf{p}_1+\mathbf{p}_2|p_3 d(\cos\theta_3). \tag{B7}$$

The new expression for the collision term is

$$I = \frac{2^3 S_1 G_F^2}{(2\pi)^5 p_1}\int \frac{d^3p_2}{p_2}(P_1\cdot P_2)^2 \int d\phi_3 \int dp_3 p_3 \int_{-1}^{1} d(\cos\theta_3)\frac{1}{p_4}\delta(p_1+p_2-p_3-p_4)F(p_1,p_2,p_3,p_4) \tag{B8}$$

$$= \frac{2^3 S_1 G_F^2}{(2\pi)^5 p_1}\int \frac{d^3p_2}{p_2}(P_1\cdot P_2)^2 (2\pi)\int dp_3 p_3 \int_{u(-1)}^{u(1)}\left(-\frac{du\,p_4}{|\mathbf{p}_1+\mathbf{p}_2|p_3}\right)\frac{1}{p_4}\delta(p_1+p_2-p_3-p_4)F(p_1,p_2,p_3,p_4) \tag{B9}$$

$$\equiv \frac{2^3 S_1 G_F^2}{(2\pi)^4 p_1}\int \frac{d^3p_2}{p_2}\frac{(P_1\cdot P_2)^2}{|\mathbf{p}_1+\mathbf{p}_2|}\int dp_3 \int_a^b du\,\delta(p_1+p_2-p_3-u)F(p_1,p_2,p_3,u), \tag{B10}$$

where the limits of integration on $\int du$ are

$$a = u(1) = (|\mathbf{p}_1+\mathbf{p}_2|^2 + p_3^2 - 2|\mathbf{p}_1+\mathbf{p}_2|p_3)^{1/2} = ||\mathbf{p}_1+\mathbf{p}_2| - p_3|, \tag{B11}$$

$$b = u(-1) = (|\mathbf{p}_1+\mathbf{p}_2|^2 + p_3^2 + 2|\mathbf{p}_1+\mathbf{p}_2|p_3)^{1/2} = |\mathbf{p}_1+\mathbf{p}_2| + p_3. \tag{B12}$$

For $\int du$ to be nonzero, the argument of the delta function must vanish within the integrable domain of $\int du$, i.e.:

$$a < p_1 + p_2 - p_3 < b. \tag{B13}$$

We will solve inequality (B13) for p_3, and modify the limits of $\int dp_3$ to ensure nonzero $\int du$. We will consider two cases: $p_3 < |\mathbf{p}_1+\mathbf{p}_2|$ and $p_3 > |\mathbf{p}_1+\mathbf{p}_2|$.

Case 1: $p_3 < |\mathbf{p}_1+\mathbf{p}_2|$. The first inequality of Eq. (B13) reads

$$|\mathbf{p}_1+\mathbf{p}_2| - p_3 < p_1 + p_2 - p_3, \tag{B14}$$

$$\Rightarrow |\mathbf{p}_1+\mathbf{p}_2| < p_1 + p_2, \tag{B15}$$

reproducing the triangle inequality which is always true. Therefore, this inequality provides no new constraints. The second inequality of Eq. (B13) reads

$$p_1 + p_2 - p_3 < |\mathbf{p}_1+\mathbf{p}_2| + p_3 \tag{B16}$$

$$\Rightarrow p_3 > \frac{1}{2}(p_1+p_2-|\mathbf{p}_1+\mathbf{p}_2|) \equiv p_{\min}. \tag{B17}$$

The possibility exists that $p_{\min} > |\mathbf{p}_1+\mathbf{p}_2|$ depending on the angle between $\mathbf{p}_1$ and $\mathbf{p}_2$. If this possibility were true, then the collision integral would vanish. Thus, the portion of the collision integral relevant to this case is

$$I_1 = \frac{2^3 S_1 G_F^2}{(2\pi)^4 p_1} \int \frac{d^3 p_2}{p_2} \frac{(P_1 \cdot P_2)^2}{|\mathbf{p}_1 + \mathbf{p}_2|} \times \int_{p_{\min}}^{p_{\mathrm{med}}} dp_3 F(p_1, p_2, p_3, p_1 + p_2 - p_3), \quad \text{(B18)}$$

where

$$p_{\mathrm{med}} = \max(p_{\min}, |\mathbf{p}_1 + \mathbf{p}_2|). \quad \text{(B19)}$$

Case 2: $p_3 > |\mathbf{p}_1 + \mathbf{p}_2|$. The first inequality of Eq. (B13) reads

$$p_3 - |\mathbf{p}_1 + \mathbf{p}_2| < p_1 + p_2 - p_3 \quad \text{(B20)}$$

$$\Rightarrow p_3 < \frac{1}{2}(p_1 + p_2 + |\mathbf{p}_1 + \mathbf{p}_2|) \equiv p_{\max}. \quad \text{(B21)}$$

$p_{\max}$ is always greater than $|\mathbf{p}_1 + \mathbf{p}_2|$. The second inequality is independent of the specific case, so $p_3 > p_{\min}$. In this case, the possibility arises that $p_{\min} > |\mathbf{p}_1 + \mathbf{p}_2|$ again, so the portion of the collision integral relevant to this case is

$$I_2 = \frac{2^3 S_1 G_F^2}{(2\pi)^4 p_1} \int \frac{d^3 p_2}{p_2} \frac{(P_1 \cdot P_2)^2}{|\mathbf{p}_1 + \mathbf{p}_2|} \times \int_{p_{\mathrm{med}}}^{p_{\max}} dp_3 F(p_1, p_2, p_3, p_1 + p_2 - p_3), \quad \text{(B22)}$$

We add I_1 to I_2 to calculate the total collision integral I. This requires the use of $p_{\min}$ and $p_{\max}$ (but not p_{med}) to set the limits of $\int dp_3$ and ensure that $\int du$ is nonzero. We write Eq. (B10) as

$$I = \frac{2^3 S_1 G_F^2}{(2\pi)^4 p_1} \int \frac{d^3 p_2}{p_2} \frac{(P_1 \cdot P_2)^2}{|\mathbf{p}_1 + \mathbf{p}_2|} \times \int_{p_{\min}}^{p_{\max}} dp_3 F(p_1, p_2, p_3, p_1 + p_2 - p_3). \quad \text{(B23)}$$

To simplify $\int d^3 p_2$, we define θ_2 to be the angle between $\mathbf{p}_1$ and $\mathbf{p}_2$. Equation (B23) becomes

$$I = \frac{2^3 S_1 G_F^2}{(2\pi)^4 p_1} \int d\phi_2 \int dp_2 p_2 \int d(\cos\theta_2) \frac{(P_1 \cdot P_2)^2}{|\mathbf{p}_1 + \mathbf{p}_2|} \int_{p_{\min}}^{p_{\max}} dp_3 F(p_1, p_2, p_3, p_1 + p_2 - p_3) \quad \text{(B24)}$$

$$= \frac{2^3 S_1 G_F^2}{(2\pi)^4 p_1} (2\pi) \int dp_2 p_2 \int d(\cos\theta_2) \frac{p_1^2 p_2^2 (1 - \cos\theta_2)^2}{(p_1^2 + p_2^2 + 2 p_1 p_2 \cos\theta_2)^{1/2}} \int_{p_{\min}}^{p_{\max}} dp_3 F(p_1, p_2, p_3, p_1 + p_2 - p_3) \quad \text{(B25)}$$

$$= \frac{2^3 S_1 G_F^2 p_1}{(2\pi)^3} \int_0^\infty dp_2 p_2^3 \int_{-1}^{1} d(\cos\theta_2) \frac{(1 - \cos\theta_2)^2}{(p_1^2 + p_2^2 + 2 p_1 p_2 \cos\theta_2)^{1/2}} \int_{p_{\min}}^{p_{\max}} dp_3 F(p_1, p_2, p_3, p_1 + p_2 - p_3). \quad \text{(B26)}$$

It will behoove us to make a change of variables on $\int d(\cos\theta_2)$. Define y such that

$$y^2 = p_1^2 + p_2^2 + 2 p_1 p_2 \cos\theta_2, \quad \text{(B27)}$$

$$\Rightarrow \cos\theta_2 = \frac{y^2 - p_1^2 - p_2^2}{2 p_1 p_2}, \quad \text{(B28)}$$

$$\Rightarrow d(\cos\theta_2) = \frac{y dy}{p_1 p_2}. \quad \text{(B29)}$$

We write Eq. (B26) as

$$I = \frac{2^3 S_1 G_F^2 p_1}{(2\pi)^3} \int_0^\infty dp_2 p_2^3 \int_{|p_1 - p_2|}^{p_1 + p_2} \frac{dy}{p_1 p_2} \left(1 - \frac{y^2 - p_1^2 - p_2^2}{2 p_1 p_2}\right)^2 \int_{p_{\min}}^{p_{\max}} dp_3 F(p_1, p_2, p_3, p_1 + p_2 - p_3) \quad \text{(B30)}$$

$$= \frac{2 S_1 G_F^2}{(2\pi)^3 p_1^2} \int_0^\infty dp_2 \int_{|p_1 - p_2|}^{p_1 + p_2} dy [(p_1 + p_2)^2 - y^2]^2 \int_{p_{\min}}^{p_{\max}} dp_3 F(p_1, p_2, p_3, p_1 + p_2 - p_3). \quad \text{(B31)}$$

Notice that the only term in the integrand of $\int dp_3$ is the occupation probability product and difference F. This term is independent of any angles, and thus independent of the integration variable y. However, the limits of $\int dp_3$ do depend on y. We define the step functions H as

$$H(x) = \begin{cases} 1 & \text{if } x > 0 \\ 0 & \text{if } x < 0 \end{cases}. \tag{B32}$$

We can rewrite $\int dp_3$ with step functions so that Eq. (B31) becomes

$$I = \frac{2S_1G_F^2}{(2\pi)^3 p_1^2}\int_0^\infty dp_2 \int_{|p_1-p_2|}^{p_1+p_2} dy[(p_1+p_2)^2-y^2]^2 \int_0^{p_1+p_2} dp_3 F(p_1,p_2,p_3,p_1+p_2-p_3)H(p_3-p_{\min})H(p_{\max}-p_3) \tag{B33}$$

$$= \frac{2S_1G_F^2}{(2\pi)^3 p_1^2}\int_0^\infty dp_2 \int_0^{p_1+p_2} dp_3 F(p_1,p_2,p_3,p_1+p_2-p_3) \int_{|p_1-p_2|}^{p_1+p_2} dy[(p_1+p_2)^2-y^2]^2 H(p_3-p_{\min})H(p_{\max}-p_3). \tag{B34}$$

For Eq. (B34) to be nonzero, the H functions must both have positive arguments. For $H(p_3 - p_{\min})$

$$p_3 - p_{\min} > 0, \tag{B35}$$

$$\Rightarrow p_3 - \frac{1}{2}(p_1+p_2-y) > 0, \tag{B36}$$

$$\Rightarrow y > p_1 + p_2 - 2p_3. \tag{B37}$$

For $H(p_{\max} - p_3)$

$$p_{\max} - p_3 > 0, \tag{B38}$$

$$\Rightarrow y > 2p_3 - p_1 - p_2. \tag{B39}$$

Conditions (B37) and (B39) imply $y > |p_1 + p_2 - 2p_3|$. p_3 is bounded above by $p_1 + p_2$, so the step functions do not modify the upper limit of $\int dy$. Let us define x_0 as the lower limit of $\int dy$. The expression for x_0 is

$$x_0 = \max(|p_1+p_2-2p_3|, |p_1-p_2|). \tag{B40}$$

If $p_1 > p_2$, then

$$x_0 = \begin{cases} p_1+p_2-2p_3 & \text{if } p_3 < p_2 \\ p_1-p_2 & \text{if } p_2 < p_3 < p_1 \\ 2p_3-p_1-p_2 & \text{if } p_3 > p_1 \end{cases}. \tag{B41}$$

If $p_1 < p_2$, then

$$x_0 = \begin{cases} p_1+p_2-2p_3 & \text{if } p_3 < p_1 \\ p_2-p_1 & \text{if } p_1 < p_3 < p_2 \\ 2p_3-p_1-p_2 & \text{if } p_3 > p_2 \end{cases}. \tag{B42}$$

Equation (B34) becomes

$$I = \frac{2S_1G_F^2}{(2\pi)^3 p_1^2}\left\{\int_0^{p_1} dp_2\left[\int_0^{p_2} dp_3 F \int_{p_1+p_2-2p_3}^{p_1+p_2} dy[(p_1+p_2)^2-y^2]^2 + \int_{p_2}^{p_1} dp_3 F \int_{p_1-p_2}^{p_1+p_2} dy[(p_1+p_2)^2-y^2]^2 + \int_{p_1}^{p_1+p_2} dp_3 F \int_{2p_3-p_1-p_2}^{p_1+p_2} dy[(p_1+p_2)^2-y^2]^2\right] + \int_{p_1}^\infty dp_2 \ldots.\right\} \tag{B43}$$

where $\int_{p_1}^\infty dp_2\ldots$ is similar to $\int_0^{p_1} dp_2$ except p_1 and p_2 are permuted in the arguments. We have dropped the arguments of F for ease in notation. Each $\int dy$ in Eq. (B43) is analytic:

$$J_1(p_1,p_2,p_3) \equiv \int_{p_1+p_2-2p_3}^{p_1+p_2} dy[(p_1+p_2)^2-y^2]^2 = \frac{16}{15}p_3^3[10(p_1+p_2)^2 - 15(p_1+p_2)p_3 + 6p_3^2], \tag{B44}$$

$$J_2(p_1,p_2) \equiv \int_{p_1-p_2}^{p_1+p_2} dy[(p_1+p_2)^2-y^2]^2 = \frac{16}{15}p_2^3[10p_1^2 + 5p_1p_2 + p_2^2], \tag{B45}$$

$$J_3(p_1,p_2,p_3) \equiv \int_{2p_3-p_1-p_2}^{p_1+p_2} dy[(p_1+p_2)^2-y^2]^2 = \frac{16}{15}[(p_1+p_2)^5 - 10(p_1+p_2)^2p_3^3 + 15(p_1+p_2)p_3^4 - 6p_3^5]. \tag{B46}$$

We are assuming that particle 1 and 2 are in the same flavor state. In this case, the symmetrization factor is $S_1 = 1/2$, and Eq. (B43) becomes

$$I = \frac{G_F^2}{(2\pi)^3 p_1^2}\left\{\int_0^{p_1} dp_2\left[\int_0^{p_2} dp_3 F J_1(p_1,p_2,p_3) + \int_{p_2}^{p_1} dp_3 F J_2(p_1,p_2) + \int_{p_1}^{p_1+p_2} dp_3 F J_3(p_1,p_2,p_3)\right]\right.$$
$$\left. + \int_{p_1}^{\infty} dp_2\left[\int_0^{p_1} dp_3 F J_1(p_1,p_2,p_3) + \int_{p_1}^{p_2} dp_3 F J_2(p_2,p_1) + \int_{p_2}^{p_1+p_2} dp_3 F J_3(p_1,p_2,p_3)\right]\right\}. \quad \text{(B47)}$$

In our nomenclature, the $\int dp_2$ in Eq. (B47) is the outer integral and the $\int dp_3$ is the inner integral. Notice that for $\int_{p_1}^{\infty} dp_2$, the arguments of J_2 and the limits of integration for each $\int dp_3$ are permuted in p_1 and p_2.

APPENDIX C: OTHER COLLISION TERMS

This appendix gives the reduction of the collision integral for the other processes in Table I. Notice that the indexing of the particle species may be different than that presented in Table I, yielding different $\langle|\mathcal{M}|^2\rangle$. We adopted the changes to simplify the mathematics involved in computing the collision integral.

1. $\nu_i + \nu_j \leftrightarrow \nu_i + \nu_j$

The summed-squared amplitude for this process is identical to the process in Appendix B except for a factor of $1/4$. Because the symmetrization factor is $S = 1$, there is an overall factor of $1/2$ on the collision integral. Therefore, the collision integral for this process has the same form as the collision integral in Appendix B.

2. $\nu_i + \bar{\nu}_i \leftrightarrow \bar{\nu}_i + \nu_i$

All of the neutrinos and antineutrinos have the same flavor for this process. We write the reaction with the following indices:

$$\nu(1) + \bar{\nu}(2) \leftrightarrow \bar{\nu}(3) + \nu(4), \quad \text{(C1)}$$

and simplify $\langle|\mathcal{M}|^2\rangle$ as

$$\langle|\mathcal{M}|^2\rangle = 2^5 G_F^2 (P_1 \cdot P_3)^2. \quad \text{(C2)}$$

The collision integral is

$$I = \frac{G_F^2}{2^2(2\pi)^3 p_1^2}\left\{\int_0^{p_1} dp_2\left[\int_0^{p_2} dp_3 F K_1(p_1,p_3) + \int_{p_2}^{p_1} dp_3 F K_2(p_1,p_2,p_3) + \int_{p_1}^{p_1+p_2} dp_3 F K_3(p_1,p_2,p_3)\right]\right.$$
$$\left. + \int_{p_1}^{\infty} dp_2\left[\int_0^{p_1} dp_3 F K_1(p_1,p_3) + \int_{p_1}^{p_2} dp_3 F K_1(p_3,p_1) + \int_{p_2}^{p_1+p_2} dp_3 F K_3(p_1,p_2,p_3)\right]\right\} \quad \text{(C3)}$$

In the above expression, $F = F(p_1,p_2,p_3,p_1+p_2-p_3)$. The K functions are the following:

$$K_1(p_1,p_3) \equiv \int_{p_1-p_3}^{p_1+p_3} dy[(p_1-p_3)^2 - y^2]^2 = \frac{16}{15} p_3^3[10p_1^2 - 5p_1p_3 + p_3^2], \quad \text{(C4)}$$

$$K_2(p_1,p_2,p_3) \equiv \int_{p_1-p_3}^{p_1+2p_2-p_3} dy[(p_1-p_3)^2 - y^2]^2 = \frac{16}{15} p_2^3[10(p_1-p_3)^2 + 15(p_1-p_3)p_2 + 6p_2^2], \quad \text{(C5)}$$

$$K_3(p_1,p_2,p_3) \equiv \int_{p_3-p_1}^{p_1+2p_2-p_3} dy[(p_1-p_3)^2 - y^2]^2 = \frac{16}{15}[(p_1-p_3)^5 + 10(p_1-p_3)^2 p_2^3 + 15(p_1-p_3)p_2^4 + 6p_2^5]. \quad \text{(C6)}$$

3. $\nu_i + \bar{\nu}_j \leftrightarrow \bar{\nu}_j + \nu_i$

In this process, the neutrino and antineutrino have different flavors. $\langle|\mathcal{M}|^2\rangle$ is identical to the process in Appendix C 2 except for a factor of $1/4$. Therefore, the collision integral for this process has the same form as the collision integral in Appendix C 2.

4. $\nu_i + \bar{\nu}_i \leftrightarrow \bar{\nu}_j + \nu_j$

In this process, a neutrino/antineutrino pair annihilate into another neutrino/antineutrino pair of different flavor. $\langle|\mathcal{M}|^2\rangle$ is identical to the process in Appendix C 3 and so the collision integral is the same.

5. $\nu_e + e^- \leftrightarrow e^- + \nu_e$

We write the reaction with the following indices:

$$\nu_e(1) + e^-(2) \leftrightarrow e^-(3) + \nu_e(4), \tag{C7}$$

and simplify $\langle|\mathcal{M}|^2\rangle$ as

$$\begin{aligned}\langle|\mathcal{M}|^2\rangle &= 2^5 G_F^2 (2\sin^2\theta_W + 1)^2 \left[(P_1\cdot Q_2)^2 - \frac{2\sin^2\theta_W}{2\sin^2\theta_W + 1} m_e^2 (P_1\cdot Q_2)\right] \\ &\quad + 2^7 G_F^2 \sin^4\theta_W \left[(P_1\cdot Q_3)^2 + \frac{2\sin^2\theta_W + 1}{2\sin^2\theta_W} m_e^2 (P_1\cdot Q_3)\right] \qquad \text{(C8)} \\ &\equiv M_1'(P_1\cdot Q_2) + M_2'(P_1\cdot Q_3). \qquad \text{(C9)}\end{aligned}$$

We will consider the collision integrals for M_1' and M_2' separately.

a. R_1 collision integral

We consider two cases for the collision integral for M_1': $p_1 < m_e/2$ and $p_1 > m_e/2$.
Case 1: $p_1 < m_e/2$. The collision integral is

$$\begin{aligned}R_1^{(1)} = \frac{1}{2^4(2\pi)^3 p_1^2}\Bigg[&\int_{m_e}^{E_{\rm cut}^{(3)}} dE_2 \left(\int_{m_e}^{E_2} dE_3 F M_1^{(1)} + \int_{E_2}^{E_{\rm trans}^{(2)}} dE_3 F M_1^{(2)} + \int_{E_{\rm trans}^{(2)}}^{E_{\rm lim}^{(1)}} dE_3 F M_1^{(3)}\right) \\ &+ \int_{E_{\rm cut}^{(3)}}^{E_{\rm cut}^{(1)}} dE_2 \left(\int_{m_e}^{E_{\rm trans}^{(2)}} dE_3 F M_1^{(1)} + \int_{E_{\rm trans}^{(2)}}^{E_2} dE_3 F M_1^{(4)} + \int_{E_2}^{E_{\rm lim}^{(1)}} dE_3 F M_1^{(3)}\right) \\ &+ \int_{E_{\rm cut}^{(1)}}^{\infty} dE_2 \left(\int_{E_{\rm lim}^{(2)}}^{E_2} dE_3 F M_1^{(4)} + \int_{E_2}^{E_{\rm lim}^{(1)}} dE_3 F M_1^{(3)}\right)\Bigg]. \qquad \text{(C10)}\end{aligned}$$

Case 2: $p_1 > m_e/2$. The collision integral is

$$\begin{aligned}R_1^{(2)} = \frac{1}{2^4(2\pi)^3 p_1^2}\Bigg[&\int_{m_e}^{E_{\rm cut}^{(3)}} dE_2 \left(\int_{m_e}^{E_2} dE_3 F M_1^{(1)} + \int_{E_2}^{E_{\rm trans}^{(2)}} dE_3 F M_1^{(2)} + \int_{E_{\rm trans}^{(2)}}^{E_{\rm lim}^{(1)}} dE_3 F M_1^{(3)}\right) \\ &+ \int_{E_{\rm cut}^{(3)}}^{\infty} dE_2 \left(\int_{m_e}^{E_{\rm trans}^{(2)}} dE_3 F M_1^{(1)} + \int_{E_{\rm trans}^{(2)}}^{E_2} dE_3 F M_1^{(4)} + \int_{E_2}^{E_{\rm lim}^{(1)}} dE_3 F M_1^{(3)}\right)\Bigg]. \qquad \text{(C11)}\end{aligned}$$

The following definitions apply to both cases:

$$F \equiv F(p_1, E_2, E_3, p_1 + E_2 - E_3), \tag{C12}$$

$$E_{\rm cut}^{(1)} \equiv m_e + \frac{2p_1^2}{m_e - 2p_1}, \tag{C13}$$

$$E_{\rm cut}^{(3)} \equiv \sqrt{p_1^2 + m_e^2}, \tag{C14}$$

$$E_{\rm trans}^{(2)} \equiv \frac{1}{2}\left(2p_1 + E_2 - q_2 + \frac{m_e^2}{2p_1 + E_2 - q_2}\right), \tag{C15}$$

$$E^{(1)}_{\rm lim} \equiv \frac{1}{2}\left(2p_1 + E_2 + q_2 + \frac{m_e^2}{2p_1 + E_2 + q_2}\right), \tag{C16}$$

$$E^{(2)}_{\rm lim} \equiv E^{(2)}_{\rm trans}, \tag{C17}$$

$$M_1^{(1)} \equiv \int_{p_1+E_2-E_3-q_3}^{p_1+E_2-E_3+q_3} dy M_1' \left\{\frac{1}{2}[(p_1+E_2)^2 - m_e^2 - y^2]\right\}, \tag{C18}$$

$$M_1^{(2)} \equiv \int_{p_1-q_2}^{p_1+q_2} dy M_1', \tag{C19}$$

$$M_1^{(3)} \equiv \int_{E_3+q_3-p_1-E_2}^{p_1+q_2} dy M_1', \tag{C20}$$

$$M_1^{(4)} \equiv \int_{q_2-p_1}^{p_1+E_2-E_3+q_3} dy M_1'. \tag{C21}$$

The argument for M_1' is the same for each $M_1^{(i)}$. The integral expressions for $M_1^{(i)}$ are all analytic, but we do not write them out here for the sake of brevity.

b. R_2 collision integral

We consider four cases for the collision integral for M_2':

$$\frac{p_1}{m_e} < \frac{\sqrt{5}-1}{4}, \tag{C22}$$

$$\frac{\sqrt{5}-1}{4} < \frac{p_1}{m_e} < \frac{1}{2\sqrt{2}}, \tag{C23}$$

$$\frac{1}{2\sqrt{2}} < \frac{p_1}{m_e} < \frac{1}{2}, \tag{C24}$$

$$\frac{1}{2} < \frac{p_1}{m_e}. \tag{C25}$$

Case 1: $p_1/m_e < (\sqrt{5}-1)/4$. The collision integral is

$$\begin{aligned} R_2^{(1)} = \frac{1}{2^4(2\pi)^3 p_1^2}\Bigg[& \int_{m_e}^{E^{(3)}_{\rm cut}} dE_3 \left(\int_{m_e}^{E_3} dE_2 F M_2^{(1)} + \int_{E_3}^{E^{(2)}_{\rm trans}} dE_2 F M_2^{(2)} + \int_{E^{(2)}_{\rm trans}}^{E^{(1)}_{\rm lim}} dE_2 F M_2^{(3)}\right) \\ & + \int_{E^{(3)}_{\rm cut}}^{E^{(2)}_{\rm cut}} dE_3 \left(\int_{m_e}^{E^{(2)}_{\rm trans}} dE_2 F M_2^{(1)} + \int_{E^{(2)}_{\rm trans}}^{E_3} dE_2 F M_2^{(4)} + \int_{E_3}^{E^{(1)}_{\rm lim}} dE_2 F M_2^{(3)}\right) \\ & + \int_{E^{(2)}_{\rm cut}}^{E^{(1)}_{\rm cut}} dE_3 \left(\int_{E^{(2)}_{\rm lim}}^{E_3} dE_2 F M_2^{(4)} + \int_{E_3}^{E^{(1)}_{\rm lim}} dE_2 F M_2^{(3)}\right) \\ & + \int_{E^{(1)}_{\rm cut}}^{\infty} dE_3 \left(\int_{E^{(2)}_{\rm lim}}^{E_3} dE_2 F M_2^{(4)} + \int_{E_3}^{\infty} dE_2 F M_2^{(3)}\right)\Bigg]. \end{aligned} \tag{C26}$$

Case 2: $(\sqrt{5}-1)/4 < p_1/m_e < 1/(2\sqrt{2})$. The collision integral is

$$\begin{aligned} R_2^{(2)} = \frac{1}{2^4(2\pi)^3 p_1^2}\Bigg[& \int_{m_e}^{E^{(3)}_{\rm cut}} dE_3 \left(\int_{m_e}^{E_3} dE_2 F M_2^{(1)} + \int_{E_3}^{E^{(2)}_{\rm trans}} dE_2 F M_2^{(2)} + \int_{E^{(2)}_{\rm trans}}^{E^{(1)}_{\rm lim}} dE_2 F M_2^{(3)}\right) \\ & + \int_{E^{(3)}_{\rm cut}}^{E^{(1)}_{\rm cut}} dE_3 \left(\int_{m_e}^{E^{(2)}_{\rm trans}} dE_2 F M_2^{(1)} + \int_{E^{(2)}_{\rm trans}}^{E_3} dE_2 F M_2^{(4)} + \int_{E_3}^{E^{(1)}_{\rm lim}} dE_2 F M_2^{(3)}\right) \\ & + \int_{E^{(1)}_{\rm cut}}^{E^{(2)}_{\rm cut}} dE_3 \left(\int_{m_e}^{E^{(2)}_{\rm trans}} dE_2 F M_2^{(1)} + \int_{E^{(2)}_{\rm trans}}^{E_3} dE_2 F M_2^{(4)} + \int_{E_3}^{\infty} dE_2 F M_2^{(3)}\right) \\ & + \int_{E^{(2)}_{\rm cut}}^{\infty} dE_3 \left(\int_{E^{(2)}_{\rm lim}}^{E_3} dE_2 F M_2^{(4)} + \int_{E_3}^{\infty} dE_2 F M_2^{(3)}\right)\Bigg]. \end{aligned} \tag{C27}$$

Case 3: $1/(2\sqrt{2}) < p_1/m_e < 1/2$. The collision integral is

$$R_2^{(3)} = \frac{1}{2^4(2\pi)^3 p_1^2}\left[\int_{m_e}^{E_{\rm cut}^{(1)}} dE_3\left(\int_{m_e}^{E_3} dE_2 F M_2^{(1)} + \int_{E_3}^{E_{\rm trans}^{(2)}} dE_2 F M_2^{(2)} + \int_{E_{\rm trans}^{(2)}}^{E_{\rm lim}^{(1)}} dE_2 F M_2^{(3)}\right)\right.$$
$$+ \int_{E_{\rm cut}^{(1)}}^{E_{\rm cut}^{(3)}} dE_3\left(\int_{m_e}^{E_3} dE_2 F M_2^{(1)} + \int_{E_3}^{E_{\rm trans}^{(2)}} dE_2 F M_2^{(2)} + \int_{E_{\rm trans}^{(2)}}^{\infty} dE_2 F M_2^{(3)}\right)$$
$$+ \int_{E_{\rm cut}^{(3)}}^{E_{\rm cut}^{(2)}} dE_3\left(\int_{m_e}^{E_{\rm trans}^{(2)}} dE_2 F M_2^{(1)} + \int_{E_{\rm trans}^{(2)}}^{E_3} dE_2 F M_2^{(4)} + \int_{E_3}^{\infty} dE_2 F M_2^{(3)}\right)$$
$$\left. + \int_{E_{\rm cut}^{(2)}}^{\infty} dE_3\left(\int_{E_{\rm lim}^{(2)}}^{E_3} dE_2 F M_2^{(4)} + \int_{E_3}^{\infty} dE_2 F M_2^{(3)}\right)\right]. \tag{C28}$$

Case 4: $p_1/m_e > 1/2$. The collision integral is

$$R_2^{(4)} = \frac{1}{2^4(2\pi)^3 p_1^2}\left[\int_{m_e}^{E_{\rm cut}^{(1)}} dE_3\left(\int_{m_e}^{E_3} dE_2 F M_2^{(1)} + \int_{E_3}^{\infty} dE_2 F M_2^{(2)}\right)\right.$$
$$+ \int_{E_{\rm cut}^{(1)}}^{E_{\rm cut}^{(3)}} dE_3\left(\int_{m_e}^{E_3} dE_2 F M_2^{(1)} + \int_{E_3}^{E_{\rm trans}^{(2)}} dE_2 F M_2^{(2)} + \int_{E_{\rm trans}^{(2)}}^{\infty} dE_2 F M_2^{(3)}\right)$$
$$+ \int_{E_{\rm cut}^{(3)}}^{E_{\rm cut}^{(2)}} dE_3\left(\int_{m_e}^{E_{\rm trans}^{(2)}} dE_2 F M_2^{(1)} + \int_{E_{\rm trans}^{(2)}}^{E_3} dE_2 F M_2^{(4)} + \int_{E_3}^{\infty} dE_2 F M_2^{(3)}\right)$$
$$\left. + \int_{E_{\rm cut}^{(2)}}^{\infty} dE_3\left(\int_{E_{\rm lim}^{(2)}}^{E_3} dE_2 F M_2^{(4)} + \int_{E_3}^{\infty} dE_2 F M_2^{(3)}\right)\right]. \tag{C29}$$

The following definitions apply to all cases. Note that some of the below definitions are incongruous with the definitions for R_1:

$$F \equiv F(p_1, E_2, E_3, p_1 + E_2 - E_3), \tag{C30}$$

$$E_{\rm cut}^{(1)} \equiv p_1 + \frac{m_e^2}{4p_1}, \tag{C31}$$

$$E_{\rm cut}^{(2)} \equiv p_1 + m_e\frac{p_1 + m_e}{2p_1 + m_e}, \tag{C32}$$

$$E_{\rm cut}^{(3)} \equiv \sqrt{p_1^2 + m_e^2}, \tag{C33}$$

$$E_{\rm trans}^{(2)} \equiv \frac{1}{2}\left(E_3 + q_3 - 2p_1 + \frac{m_e^2}{E_3 + q_3 - 2p_1}\right), \tag{C34}$$

$$E_{\rm lim}^{(1)} \equiv \frac{1}{2}\left(E_3 - q_3 - 2p_1 + \frac{m_e^2}{E_3 - q_3 - 2p_1}\right), \tag{C35}$$

$$E_{\rm lim}^{(2)} \equiv E_{\rm trans}^{(2)}, \tag{C36}$$

$$M_2^{(1)} \equiv \int_{p_1 - E_3 + E_2 - q_2}^{p_1 - E_3 + E_2 + q_2} dy M_2'\left\{\frac{1}{2}[y^2 + m_e^2 - (p_1 - E_3)^2]\right\}, \tag{C37}$$

$$M_2^{(2)} \equiv \int_{p_1 - q_3}^{p_1 + q_3} dy M_2', \tag{C38}$$

$$M_2^{(3)} \equiv \int_{E_3 - p_1 - E_2 + q_2}^{p_1 + q_3} dy M_2', \tag{C39}$$

$$M_2^{(4)} \equiv \int_{q_3 - p_1}^{p_1 - E_3 + E_2 + q_2} dy M_2'. \tag{C40}$$

6. $\nu_{\mu(\tau)} + e^- \leftrightarrow e^- + \nu_{\mu(\tau)}$

The $\langle|\mathcal{M}|^2\rangle$ in this case is identical to the $\langle|\mathcal{M}|^2\rangle$ in Appendix C 5, except for the transformation $2\sin^2\theta_W + 1 \to 2\sin^2\theta_W - 1$. Therefore, the structure of the collision integral for this process is the same as Appendix C 5.

7. $\nu_e + e^+ \leftrightarrow e^+ + \nu_e$

We write the reaction with the following indices:

$$\nu_e(1) + e^+(2) \leftrightarrow e^+(3) + \nu_e(4), \tag{C41}$$

and simplify $\langle|\mathcal{M}|^2\rangle$ as

$$\langle|\mathcal{M}|^2\rangle = 2^5 G_F^2 (2\sin^2\theta_W + 1)^2 \left[(P_1\cdot Q_3)^2 - \frac{2\sin^2\theta_W}{2\sin^2\theta_W + 1} m_e^2 (P_1\cdot Q_3)\right] + 2^7 G_F^2 \sin^4\theta_W \left[(P_1\cdot Q_2)^2 + \frac{2\sin^2\theta_W + 1}{2\sin^2\theta_W} m_e^2 (P_1\cdot Q_2)\right] \tag{C42}$$

$$= M_1'(P_1\cdot Q_3) + M_2'(P_1\cdot Q_2), \tag{C43}$$

where M_1' and M_2' are the same functions as in Appendix C 5. Therefore, we can use the same collision integrals as Appendix C 5 but use M_2' in the integrands of R_1, and M_1' in the integrands of R_2.

8. $\nu_{\mu(\tau)} + e^+ \leftrightarrow e^+ + \nu_{\mu(\tau)}$

The $\langle|\mathcal{M}|^2\rangle$ is the same as in Appendix C 7 except for the transformation $2\sin^2\theta_W + 1 \to 2\sin^2\theta_W - 1$. Therefore, the structure of the collision integral for this process is the same as Appendix C 7.

9. $\nu_e + \bar{\nu}_e \leftrightarrow e^- + e^+$

We write the reaction with the following indices:

$$\nu_e(1) + \bar{\nu}_e(4) \leftrightarrow e^+(2) + e^-(3), \tag{C44}$$

and simplify $\langle|\mathcal{M}|^2\rangle$ as

$$\langle|\mathcal{M}|^2\rangle = 2^5 G_F^2 (1 + 2\sin^2\theta_W)^2 \left[(P_1\cdot Q_2)^2 + \frac{2\sin^2\theta_W}{1 + 2\sin^2\theta_W} m_e^2 (P_1\cdot Q_2)\right] + 2^7 G_F^2 \sin^4\theta_W \left[(P_1\cdot Q_3)^2 + \frac{1 + 2\sin^2\theta_W}{2\sin^2\theta_W} m_e^2 (P_1\cdot Q_3)\right] \tag{C45}$$

$$\equiv L_1'(P_1\cdot Q_2) + L_2'(P_1\cdot Q_3). \tag{C46}$$

We consider four cases for the collision integral:

$$\frac{p_1}{m_e} < \frac{1}{2}, \tag{C47}$$

$$\frac{1}{2} < \frac{p_1}{m_e} < \frac{1+\sqrt{5}}{4}, \tag{C48}$$

$$\frac{1+\sqrt{5}}{4} < \frac{p_1}{m_e} < 1, \tag{C49}$$

$$1 < \frac{p_1}{m_e}. \tag{C50}$$

Case 1: $p_1/m_e < 1/2$. The collision integral is

$$I^{(1)} = \frac{1}{2^4(2\pi)^3 p_1^2}\int_{E_{\rm cut}^{(1)}}^{\infty} dE_{\rm out}\int_{E_{\rm lim}^{(1)}}^{\infty} dE_{\rm in}(F_{oi}L_1^{(1)} + F_{io}L_2^{(1)}). \tag{C51}$$

Case 2: $1/2 < p_1/m_e < \frac{1+\sqrt{5}}{4}$. The collision integral is

$$\begin{aligned} I^{(2)} = \frac{1}{2^4(2\pi)^3 p_1^2}\Bigg\{ & \int_{m_e}^{E_{\rm cut}^{(1)}} dE_{\rm out}\left[\int_{E_{\rm lim}^{(1)}}^{E_{\rm trans}^{(1)}} dE_{\rm in}(F_{oi}L_1^{(1)} + F_{io}L_2^{(1)}) + \int_{E_{\rm trans}^{(1)}}^{\infty} dE_{\rm in}(F_{oi}L_1^{(2)} + F_{io}L_2^{(2)})\right] \\ & + \int_{E_{\rm cut}^{(1)}}^{E_{\rm cut}^{(2)}} dE_{\rm out}\left[\int_{E_{\rm lim}^{(1)}}^{\infty} dE_{\rm in}(F_{oi}L_1^{(1)} + F_{io}L_2^{(1)})\right] \\ & + \int_{E_{\rm cut}^{(2)}}^{\infty} dE_{\rm out}\left[\int_{m_e}^{E_{\rm trans}^{(2)}} dE_{\rm in}(F_{oi}L_1^{(3)} + F_{io}L_2^{(3)}) + \int_{E_{\rm trans}^{(2)}}^{\infty} dE_{\rm in}(F_{oi}L_1^{(1)} + F_{io}L_2^{(1)})\right]\Bigg\}. \end{aligned} \tag{C52}$$

Case 3: $\frac{1+\sqrt{5}}{4} < p_1/m_e < 1$. The collision integral is

$$\begin{aligned} I^{(3)} = \frac{1}{2^4(2\pi)^3 p_1^2}\Bigg\{ & \int_{m_e}^{E_{\rm cut}^{(2)}} dE_{\rm out}\left[\int_{E_{\rm lim}^{(1)}}^{E_{\rm trans}^{(1)}} dE_{\rm in}(F_{oi}L_1^{(1)} + F_{io}L_2^{(1)}) + \int_{E_{\rm trans}^{(1)}}^{\infty} dE_{\rm in}(F_{oi}L_1^{(2)} + F_{io}L_2^{(2)})\right] \\ & + \int_{E_{\rm cut}^{(2)}}^{E_{\rm cut}^{(1)}} dE_{\rm out}\left[\int_{m_e}^{E_{\rm trans}^{(2)}} dE_{\rm in}(F_{oi}L_1^{(3)} + F_{io}L_2^{(3)}) + \int_{E_{\rm trans}^{(2)}}^{E_{\rm trans}^{(1)}} dE_{\rm in}(F_{oi}L_1^{(1)} + F_{io}L_2^{(1)}) + \int_{E_{\rm trans}^{(1)}}^{\infty} dE_{\rm in}(F_{oi}L_1^{(2)} + F_{io}L_2^{(2)})\right] \\ & + \int_{E_{\rm cut}^{(1)}}^{\infty} dE_{\rm out}\left[\int_{m_e}^{E_{\rm trans}^{(2)}} dE_{\rm in}(F_{oi}L_1^{(3)} + F_{io}L_2^{(3)}) + \int_{E_{\rm trans}^{(2)}}^{\infty} dE_{\rm in}(F_{oi}L_1^{(1)} + F_{io}L_2^{(1)})\right]\Bigg\}. \end{aligned} \tag{C53}$$

Case 4: $p_1/m_e > 1$. The collision integral is

$$\begin{aligned} I^{(4)} = \frac{1}{2^4(2\pi)^3 p_1^2}\Bigg\{ & \int_{m_e}^{E_{\rm cut}^{(2)}} dE_{\rm out}\left[\int_{E_{\rm lim}^{(2)}}^{E_{\rm trans}^{(2)}} dE_{\rm in}(F_{oi}L_1^{(4)} + F_{io}L_2^{(4)}) + \int_{E_{\rm trans}^{(2)}}^{\infty} dE_{\rm in}(F_{oi}L_1^{(2)} + F_{io}L_2^{(2)})\right] \\ & + \int_{E_{\rm cut}^{(2)}}^{p_1} dE_{\rm out}\left[\int_{m_e}^{E_{\rm trans}^{(1)}} dE_{\rm in}(F_{oi}L_1^{(3)} + F_{io}L_2^{(3)}) + \int_{E_{\rm trans}^{(1)}}^{E_{\rm trans}^{(2)}} dE_{\rm in}(F_{oi}L_1^{(4)} + F_{io}L_2^{(4)}) + \int_{E_{\rm trans}^{(2)}}^{\infty} dE_{\rm in}(F_{oi}L_1^{(2)} + F_{io}L_2^{(2)})\right] \\ & + \int_{p_1}^{E_{\rm cut}^{(1)}} dE_{\rm out}\left[\int_{m_e}^{E_{\rm trans}^{(2)}} dE_{\rm in}(F_{oi}L_1^{(3)} + F_{io}L_2^{(3)}) + \int_{E_{\rm trans}^{(2)}}^{E_{\rm trans}^{(1)}} dE_{\rm in}(F_{oi}L_1^{(1)} + F_{io}L_2^{(1)}) + \int_{E_{\rm trans}^{(1)}}^{\infty} dE_{\rm in}(F_{oi}L_1^{(2)} + F_{io}L_2^{(2)})\right] \\ & + \int_{E_{\rm cut}^{(1)}}^{\infty} dE_{\rm out}\left[\int_{m_e}^{E_{\rm trans}^{(2)}} dE_{\rm in}(F_{oi}L_1^{(3)} + F_{io}L_2^{(3)}) + \int_{E_{\rm trans}^{(2)}}^{\infty} dE_{\rm in}(F_{oi}L_1^{(1)} + F_{io}L_2^{(1)})\right]\Bigg\}. \end{aligned} \tag{C54}$$

The above expressions use the following definitions:

$$q_{\rm out} \equiv \sqrt{E_{\rm out}^2 - m_e^2}, \tag{C55}$$

$$q_{\rm in} \equiv \sqrt{E_{\rm in}^2 - m_e^2}, \tag{C56}$$

$$F_{oi} \equiv F(p_1, E_{\rm out} + E_{\rm in} - p_1, E_{\rm out}, E_{\rm in}), \tag{C57}$$

$$F_{io} \equiv F(p_1, E_{\rm out} + E_{\rm in} - p_1, E_{\rm in}, E_{\rm out}), \tag{C58}$$

$$E_{\rm cut}^{(1)} \equiv p_1 + \frac{m_e^2}{4p_1}, \tag{C59}$$

$$E_{\rm cut}^{(2)} \equiv \frac{1}{2}\left(2p_1 - m_e + \frac{m_e^2}{2p_1 - m_e}\right), \tag{C60}$$

$$E_{\rm trans}^{(1)} \equiv \frac{1}{2}\left(2p_1 - E_{\rm out} - q_{\rm out} + \frac{m_e^2}{2p_1 - E_{\rm out} - q_{\rm out}}\right), \tag{C61}$$

$$E_{\rm trans}^{(2)} \equiv \frac{1}{2}\left(2p_1 - E_{\rm out} + q_{\rm out} + \frac{m_e^2}{2p_1 - E_{\rm out} + q_{\rm out}}\right), \tag{C62}$$

$$E_{\rm lim}^{(1)} \equiv E_{\rm trans}^{(2)}, \tag{C63}$$

$$E_{\rm lim}^{(2)} \equiv E_{\rm trans}^{(1)}, \tag{C64}$$

and

$$L_1^{(1)} \equiv \int_{E_{\rm out}-p_1+E_{\rm in}-q_{\rm in}}^{p_1+q_{\rm out}} dy L_1' \left\{\frac{1}{2}[y^2 + m_e^2 - (p_1 - E_{\rm out})^2]\right\}, \tag{C65}$$

$$L_1^{(2)} \equiv \int_{p_1-q_{\rm out}}^{p_1+q_{\rm out}} dy L_1', \tag{C66}$$

$$L_1^{(3)} \equiv \int_{E_{\rm out}-p_1+E_{\rm in}-q_{\rm in}}^{E_{\rm out}-p_1+E_{\rm in}+q_{\rm in}} dy L_1', \tag{C67}$$

$$L_1^{(4)} \equiv \int_{p_1-q_{\rm out}}^{E_{\rm out}-p_1+E_{\rm in}+q_{\rm in}} dy L_1', \tag{C68}$$

$$L_2^{(1)} \equiv \int_{E_{\rm out}-p_1+E_{\rm in}-q_{\rm in}}^{p_1+q_{\rm out}} dy L_2' \left\{\frac{1}{2}[y^2 + m_e^2 - (p_1 - E_{\rm out})^2]\right\}, \tag{C69}$$

$$L_2^{(2)} \equiv \int_{p_1-q_{\rm out}}^{p_1+q_{\rm out}} dy L_2', \tag{C70}$$

$$L_2^{(3)} \equiv \int_{E_{\rm out}-p_1+E_{\rm in}-q_{\rm in}}^{E_{\rm out}-p_1+E_{\rm in}+q_{\rm in}} dy L_2', \tag{C71}$$

$$L_2^{(4)} \equiv \int_{p_1-q_{\rm out}}^{E_{\rm out}-p_1+E_{\rm in}+q_{\rm in}} dy L_2'. \tag{C72}$$

10. $\nu_{\mu(\tau)} + \bar{\nu}_{\mu(\tau)} \leftrightarrow e^- + e^+$

The $\langle|\mathcal{M}|^2\rangle$ is the same as in Appendix C 9 except for the transformation $2\sin^2\theta_W + 1 \to 2\sin^2\theta_W - 1$. Therefore, the structure of the collision integral for this process is the same as Appendix C 9.

[1] D. A. Dicus, E. W. Kolb, A. M. Gleeson, E. C. G. Sudarshan, V. L. Teplitz, and M. S. Turner, Primordial nucleosynthesis including radiative, Coulomb, and finite-temperature corrections to weak rates, Phys. Rev. D **26**, 2694 (1982).

[2] J.-L. Cambier, J. R. Primack, and M. Sher, Finite temperature radiative corrections to neutron decay and related processes, Nucl. Phys. **B209**, 372 (1982).

[3] M. A. Herrera and S. Hacyan, Relaxation time of neutrinos in the early universe, Astrophys. J. **336**, 539 (1989).

[4] N. C. Rana and B. Mitra, Effect of neutrino heating in the early Universe on neutrino decoupling temperatures and nucleosynthesis, Phys. Rev. D **44**, 393 (1991).

[5] S. Dodelson and M. S. Turner, Nonequilibrium neutrino statistical mechanics in the expanding Universe, Phys. Rev. D **46**, 3372 (1992).

[6] S. Hannestad and J. Madsen, Neutrino decoupling in the early Universe, Phys. Rev. D **52**, 1764 (1995).

[7] A. D. Dolgov, S. H. Hansen, and D. V. Semikoz, Non-equilibrium corrections to the spectra of massless neutrinos in the early universe, Nucl. Phys. **B503**, 426 (1997).

[8] N. Y. Gnedin and O. Y. Gnedin, Cosmological Neutrino Background Revisited, Astrophys. J. **509**, 11 (1998).

[9] A. D. Dolgov, S. H. Hansen, and D. V. Semikoz, Non-equilibrium corrections to the spectra of massless neutrinos in the early universe, Nucl. Phys. **B543**, 269 (1999).

[10] R. E. Lopez and M. S. Turner, Precision prediction for the big-bang abundance of primordial ^{4}He, Phys. Rev. D **59**, 103502 (1999).

[11] S. Esposito, G. Miele, S. Pastor, M. Peloso, and O. Pisanti, Non equilibrium spectra of degenerate relic neutrinos, Nucl. Phys. **B590**, 539 (2000).

[12] G. Mangano, G. Miele, S. Pastor, and M. Peloso, A precision calculation of the effective number of cosmological neutrinos, Phys. Lett. B **534**, 8 (2002).

[13] G. Mangano, G. Miele, S. Pastor, T. Pinto, O. Pisanti, and P. D. Serpico, Relic neutrino decoupling including flavour oscillations, Nucl. Phys. **B729**, 221 (2005).

[14] J. Birrell, C. T. Yang, and J. Rafelski, Relic neutrino freeze-out: Dependence on natural constants, Nucl. Phys. **B890**, 481 (2015).

[15] K. N. Abazajian, K. Arnold, J. Austermann, B. A. Benson, C. Bischoff, J. Bock, J. R. Bond, J. Borrill, E. Calabrese, J. E. Carlstrom *et al.*, Neutrino physics from the cosmic microwave background and large scale structure, Astropart. Phys. **63**, 66 (2015).

[16] D. Silva, P. Hickson, C. Steidel, and M. Bolte, TMT Detailed Science Case: 2007, http://www.tmt.org.

[17] P. McCarthy and R. A. Bernstein, Giant Magellan Telescope: Status and Opportunities for Scientific Synergy, in *Thirty Meter Telescope Science Forum, 2014, Tucson, Arizona*, p. 61, http://conference.ipac.caltech.edu/tmtsf2014.

[18] *The Science Case for the European Extremely Large Telescope: The Next Step in Mankind's Quest for the Universe*, edited by I. Hook (OPTICON, Cambridge, England, and European Southern Observatory (ESO), Garching bei Muenchen, Germany, 2005).

[19] G. M. Fuller, C. T. Kishimoto, and A. Kusenko, Heavy sterile neutrinos, entropy and relativistic energy production, and the relic neutrino background, arXiv:1110.6479.

[20] K. M. Nollett and G. Steigman, BBN and the CMB constrain neutrino coupled light WIMPs, Phys. Rev. D **91**, 083505 (2015).

[21] N. Vassh, E. Grohs, A. B. Balantekin, and G. M. Fuller, Majorana neutrino magnetic moment and neutrino decoupling in big bang nucleosynthesis, Phys. Rev. D **92**, 125020 (2015).

[22] E. W. Kolb and M. S. Turner, *The Early Universe* (Addison-Wesley Publishing Co., New York, 1990).

[23] S. Dodelson, *Modern Cosmology* (Academic Press, New York, 2003).

[24] S. Weinberg, *Cosmology* (Oxford University Press, New York, 2008).

[25] A. Vlasenko, G. M. Fuller, and V. Cirigliano, Neutrino quantum kinetics, Phys. Rev. D **89**, 105004 (2014).

[26] R. Barbieri and A. Dolgov, Neutrino oscillations in the early universe, Nucl. Phys. **B349**, 743 (1991).

[27] E. K. Akhmedov and Z. G. Berezhiani, Implications of Majorana neutrino transition magnetic moments for neutrino signals from supernovae, Nucl. Phys. **B373**, 479 (1992).

[28] G. Raffelt and G. Sigl, Neutrino flavor conversion in a supernova core, Astropart. Phys. **1**, 165 (1993).

[29] P. Strack and A. Burrows, Generalized Boltzmann formalism for oscillating neutrinos, Phys. Rev. D **71**, 093004 (2005).

[30] A. B. Balantekin and Y. Pehlivan, Neutrino neutrino interactions and flavour mixing in dense matter, J. Phys. G **34**, 47 (2007).

[31] C. Volpe, D. Väänänen, and C. Espinoza, Extended evolution equations for neutrino propagation in astrophysical and cosmological environments, Phys. Rev. D **87**, 113010 (2013).

[32] A. B. Balantekin and G. M. Fuller, Neutrinos in cosmology and astrophysics, Prog. Part. Nucl. Phys. **71**, 162 (2013).

[33] A. de Gouvêa and S. Shalgar, Transition magnetic moments and collective neutrino oscillations: three-flavor effects and detectability, J. Cosmol. Astropart. Phys. 4 (2013) 018.

[34] J. Serreau and C. Volpe, Neutrino-antineutrino correlations in dense anisotropic media, Phys. Rev. D **90**, 125040 (2014).

[35] V. Cirigliano, G. M. Fuller, and A. Vlasenko, A new spin on neutrino quantum kinetics, Phys. Lett. B **747**, 27 (2015).

[36] R. V. Wagoner, Synthesis of the elements within objects exploding from very high temperatures, Astrophys. J. Suppl. Ser. **18**, 247 (1969).

[37] M. S. Smith, L. H. Kawano, and R. A. Malaney, Experimental, computational, and observational analysis of primordial nucleosynthesis, Astrophys. J. Suppl. Ser. **85**, 219 (1993).

[38] R. N. Boyd, C. R. Brune, G. M. Fuller, and C. J. Smith, New nuclear physics for big bang nucleosynthesis, Phys. Rev. D **82**, 105005 (2010).

[39] E. Grohs, G. M. Fuller, C. T. Kishimoto, and M. W. Paris, Probing neutrino physics with a self-consistent treatment of the weak decoupling, nucleosynthesis, and photon decoupling epochs, J. Cosmol. Astropart. Phys. 5 (2015) 17.

[40] D. L. Tubbs and D. N. Schramm, Neutrino opacities at high temperatures and densities, Astrophys. J. **201**, 467 (1975).

[41] E. G. Flowers and P. G. Sutherland, Neutrino-neutrino scattering and supernovae, Astrophys. J. Lett. **208**, L19 (1976).

[42] S. Elhay and J. Kautsky, Algorithm 655: Iqpack: Fortran subroutines for the weights of interpolatory quadratures, ACM Trans. Math. Softw. **13**, 399 (1987).

[43] W. H. Press, S. A. Teukolsky, W. T. Vetterling, and B. P. Flannery, *Numerical Recipes in FORTRAN*, The Art of Scientific Computing, 2nd ed. (Cambridge University Press, New York, 1993).

[44] A. F. Heckler, Astrophysical applications of quantum corrections to the equation of state of a plasma, Phys. Rev. D **49**, 611 (1994).

[45] N. Fornengo, C. W. Kim, and J. Song, Finite temperature effects on the neutrino decoupling in the early Universe, Phys. Rev. D **56**, 5123 (1997).

[46] J. Bernstein, *Kinetic Theory in the Expanding Universe* (Cambridge University Press, Cambridge/New York, 1988).

[47] P. A. R. Ade *et al.* (Planck Collaboration), Planck 2013 results. XVI. Cosmological parameters, Astron. Astrophys. **571**, A16 (2014).

[48] R. V. Wagoner, W. A. Fowler, and F. Hoyle, On the synthesis of elements at very high temperature, Astrophys. J. **148**, 3 (1967).

[49] G. M. Fuller, W. A. Fowler, and M. J. Newman, Stellar weak-interaction rates for sd-shell nuclei. I - Nuclear matrix element systematics with application to Al-26 and selected nuclei of importance to the supernova problem, Astrophys. J. Suppl. Ser. **42**, 447 (1980).

[50] C. J. Smith and G. M. Fuller, Weak interaction rate Coulomb corrections in big bang nucleosynthesis, Phys. Rev. D **81**, 065027 (2010).

[51] O. Pisanti, A. Cirillo, S. Esposito, F. Iocco, G. Mangano, G. Miele, and P. D. Serpico, PArthENoPE: Public algorithm evaluating the nucleosynthesis of primordial elements, Comput. Phys. Commun. **178**, 956 (2008).

[52] K. M. Nollett and G. Steigman, BBN and the CMB constrain light, electromagnetically coupled WIMPs, Phys. Rev. D **89**, 083508 (2014).

[53] L. Kawano, Let's go: Early universe 2. Primordial nucleosynthesis the computer way, No. 92, NASA STI/Recon Technical Report, United States, 1992.

[54] E. G. Adelberger *et al.*, Solar fusion cross sections. II. The pp chain and CNO cycles, Rev. Mod. Phys. **83**, 195 (2011).

[55] L. E. Marcucci, G. Mangano, A. Kievsky, and M. Viviani, Implication of the Proton-Deuteron Radiative Capture for Big Bang Nucleosynthesis, Phys. Rev. Lett. **116**, 102501 (2016).

[56] D. Tytler, J. M. O'Meara, N. Suzuki, and D. Lubin, Deuterium and the baryonic density of the universe, Phys. Rep. **333**, 409 (2000).

[57] D. Kirkman, D. Tytler, N. Suzuki, J. M. O'Meara, and D. Lubin, The cosmological baryon density from the deuterium-to-hydrogen ratio in QSO absorption systems: D/H toward $Q1243+3047$, Astrophys. J. Suppl. Ser. **149**, 1 (2003).

[58] M. Pettini and R. Cooke, A new, precise measurement of the primordial abundance of deuterium, Mon. Not. R. Astron. Soc. **425**, 2477 (2012).

[59] R. J. Cooke, M. Pettini, R. A. Jorgenson, M. T. Murphy, and C. C. Steidel, Precision measures of the primordial abundance of deuterium, Astrophys. J. **781**, 31 (2014).

[60] C. J. Smith, G. M. Fuller, and M. S. Smith, Big bang nucleosynthesis with independent neutrino distribution functions, Phys. Rev. D **79**, 105001 (2009).

[61] J. L. Menestrina and R. J. Scherrer, Dark radiation from particle decays during big bang nucleosynthesis, Phys. Rev. D **85**, 047301 (2012).

[62] K. Jedamzik, G. M. Fuller, and G. J. Mathews, Inhomogeneous primordial nucleosynthesis: Coupled nuclear reactions and hydrodynamic dissipation processes, Astrophys. J. **423**, 50 (1994).

[63] S. G. Ryan, T. C. Beers, K. A. Olive, B. D. Fields, and J. E. Norris, Primordial lithium and big bang nucleosynthesis, Astrophys. J. Lett. **530**, L57 (2000).

[64] K. Abazajian, N. F. Bell, G. M. Fuller, and Y. Y. Y. Wong, Cosmological lepton asymmetry, primordial nucleosynthesis and sterile neutrinos, Phys. Rev. D **72**, 063004 (2005).

[65] A. de Gouvea *et al.*, Neutrinos, arXiv:1310.4340.